

This manuscript is titled '**Ocean-bottom Seismic Interferometry in Coupled Acoustic-Elastic Media**' with authors: **Adesh Pandey** (adesh0805@gmail.com), **Sjoerd de Ridder** (S.Deridder@leeds.ac.uk), **Jeffrey Shragge** (jshragge@gmail.com), and **Aaron J. Girard** (aaron.j.girard@gmail.com). It has been submitted for review in **Geophysical Journal International**.

Please note that while this manuscript is undergoing peer-review, it has not been accepted for publication at the time of submission to EarthArxiv. Subsequent versions of the manuscript may have slightly different content. If accepted, the final version of this manuscript will be available via the 'Peer-reviewed Publication DOI' link on the EarthArxiv posting page. Please feel free to contact any authors with feedback.

1 Ocean-bottom Seismic Interferometry in Coupled 2 Acoustic-Elastic Media

3 Adesh Pandey¹, Sjoerd de Ridder², Jeffrey Shragge¹, and Aaron J. Girard¹

¹ *Center for Wave Phenomena, Department of Geophysics, Colorado School of Mines, Golden CO 80401, USA*

² *School of Earth and Environment, University of Leeds, Leeds, UK*

4 5 SUMMARY

6 Green's function expressions for seismic interferometry in acoustic and elastic media
7 have been extensively studied and applied across a wide range of applications, includ-
8 ing surface-wave tomography and generating virtual shot gathers. However, analogous
9 expressions for coupled acoustic-elastic media systems remain absent, despite their im-
10 portance for analysing cross-correlation wavefields from ocean-bottom nodal and seis-
11 mometer recordings and other seismic problems in marine settings. To address this is-
12 sue, we derive convolution- and correlation-type reciprocity relations for physically cou-
13 pled acoustic-elastic media by combining Rayleigh's and Rayleigh-Betti reciprocity the-
14 orems, incorporating the constitutive equations governing coupling at the acoustic-elastic
15 interface, and applying time-reversal invariance principles for an arbitrary 3-D inhom-
16 geneous, lossless medium. The derived relationships show that the acoustic and elastic
17 Green's functions between any two observation points in the medium can be expressed
18 as integrals of cross-correlations of wavefield observations at those locations, generated
19 by sources distributed over an arbitrarily shaped closed surface enclosing the two obser-
20 vation points. When the Earth's free surface coincides with the enclosing surface, inte-
21 gral evaluation is required only over the remaining portion of the closed surface. If the
22 sources are mutually uncorrelated ambient sources, the Green's function representation

23 simplifies to a direct cross-correlation of wavefield observations at the two points, gener-
24 ated by a specific ambient source distribution on the closed surface. However, in practical
25 scenarios, the ideal source distribution necessary to retrieve Green's functions is rarely
26 realized, for example, due to non-uniform illumination. To address these challenges, we
27 represent the ambient cross-correlations as self-consistent observations and introduce a
28 cross-correlation modelling methodology that accounts for practical limitations in source
29 distribution for coupled acoustic-elastic media scenarios. We illustrate the theory by mod-
30 elling ambient cross-correlation wavefields for a deep-water scenario.

31 **1 INTRODUCTION**

32 Recent advances in sparse, large-scale, multi-component ocean-bottom sensor array deployments –
33 including ocean-bottom seismometers (OBSs), cables (OBCs), and nodes (OBNs) – offer a unique
34 opportunity to enhance our understanding of marine ambient wavefield phenomena by extracting low-
35 frequency (sub-2.0 Hz) wavefield information at the seabed. Many continuous ocean-bottom acqui-
36 sitions lasting for durations spanning one to three months are designed for active-source seismic ex-
37 ploration, where short-duration windows are extracted to form shot gathers, with the remainder of the
38 data archived and often disregarded as containing little useful information for subsurface investigation
39 - especially below the 2.0 Hz low-frequency cutoff of typical marine air-gun sources.

40 Long-time continuous seafloor recordings, though, also capture a rich broadband spectrum of am-
41 bient seismic energy in the 0.01-1.0 Hz frequency range, and a growing number of studies demonstrate
42 that this low-frequency energy can be transformed into useful surface-wave information through seis-
43 mic interferometry (de Ridder & Dellinger 2011; Girard et al. 2023, 2024). For example, ambient
44 virtual shot gather (VSG) volumes derived from continuous wavefield data recorded on OBC arrays at
45 the Valhall (de Ridder & Dellinger 2011) and Ekofisk (de Ridder & Biondi 2015) fields in the Norwe-
46 gian North Sea, as well as OBN arrays in the Gulf of Mexico (Stewart 2006; Girard et al. 2023, 2024),
47 reveal dispersive surface- and guided P-wave modes. These VSGs also exhibit surface-wave sensitiv-
48 ity to strong lateral velocity heterogeneities (e.g., salt bodies) within the sub-2.0 Hz frequency band.
49 de Ridder & Dellinger (2011) further used VSG data for ambient eikonal tomography to perform
50 near-seabed imaging at the North Sea Valhall field, while de Ridder & Biondi (2015) used VSG-
51 derived dispersion panels to image Scholte-wave group velocities via straight-ray tomography. These
52 examples demonstrate the potential of using the low-frequency information recorded on ocean-bottom
53 sensors for subsurface investigation, complementing conventional exploration methods.

54 To fully exploit the potential of ambient VSG data and move toward low-frequency elastic Earth
55 model building through full-waveform inversion (FWI), it is essential to understand the physical sig-
56 nificance of the cross-correlated wavefield recorded on ocean-bottom sensors. This understanding re-
57 quires interpreting ambient wavefield information within the context of marine settings characterized
58 by physically coupled acoustic-elastic media and accurately modelling these wavefields for FWI work-
59 flows within an appropriate seismic interferometry (SI) framework. Consequently, it is imperative to
60 develop Green’s function representations for SI in such coupled-media systems, to understand when
61 the underlying assumptions are realized, and to develop methodologies for using approximate repre-
62 sentations for SI when they are not.

63 In SI, waves recorded at two receiver locations are correlated to approximate Green’s function be-
64 tween these locations. Seismic wavefield energy, continuously generated by a diverse array of sources
65 – including active sources, oceanic phenomena, and localized seismic events such as earthquakes –
66 form the basis for such correlation-based interferometric analyses. Wapenaar & Fokkema (2006) pro-
67 vides a comprehensive overview of Green’s function representations in terms of cross-correlations of
68 full wavefields in arbitrary configurations (Weaver & Lobkis 2004; van Manen et al. 2006) and dis-
69 cusses modifications for their application in SI for both acoustic and elastodynamic systems, without
70 assuming wavefield diffusivity. Lobkis & Weaver (2001), Wapenaar (2004), and Wapenaar & Fokkema
71 (2006) demonstrate that the interstation correlation of ambient wavefields can approximate the inter-
72 station Green’s function under the assumption of a diffused, equipartitioned, random, and uncorrelated
73 “noise” field. Applications of Green’s function retrieval using SI in acoustic and elastic systems have
74 been extensively studied and successfully applied across various fields, including helioseismology
75 (Rickett & Claerbout 2000), ultrasonics (Lobkis & Weaver 2001) as well as exploration (Bakulin &
76 Calvert 2004) and global (Sager et al. 2018) seismology. However, Green’s function representations
77 for SI in coupled acoustic-elastic media, such as those encountered in ocean-bottom acquisition in
78 marine environments, remain poorly studied and are notably absent from the literature.

79 This paper derives reciprocity relations for coupled acoustic-elastic systems by employing consti-
80 tutive equations at the acoustic-elastic interface and reciprocity theorems for the associated acoustic
81 and elastodynamic media. We establish source-receiver reciprocity expressions and give an overview
82 of Green’s function representations for pressure and particle velocity data in such systems, expressed
83 through cross correlations of full wavefields in arbitrary configurations within inhomogeneous, loss-
84 less media. We consider both open and free-surface configurations with approximations introduced to
85 address practical SI challenges, including source availability and characteristics. For practical applica-
86 tions, we present a cross-correlation modelling (CCM) approach derived from Tromp et al. (2010) for
87 realistically representing and modelling of ambient wavefield cross correlations, supported by a syn-

thetic simulation that highlights CCM waveform differences from the corresponding direct Green's function response.

2 RECIPROCITY FOR COUPLED ACOUSTIC-ELASTIC SYSTEMS

In many applications, such as exploration focused OBN deployments or globally focused marine seismic acquisition, waves propagating in an acoustic medium are physically coupled to wave motion in the underlying elastic solid through constitutive equations (Sun et al. 2017; Sethi et al. 2021). Figure 1 illustrates the configuration of such a coupled domain where the acoustic medium, denoted as V^a , is governed by acoustic wave-equation physics while wave propagation in the underlying elastic medium, denoted as V^e , is described by the elastic wave equations.

2.1 Acoustic Region

In the acoustic region V^a , Rayleigh's reciprocity theorem as (Rayleigh 1878; de Hoop 1988; Fokkema & van den Berg 1993; Wapenaar & Fokkema 2006) is given by:

$$\begin{aligned} & \int_{V^a} \left(\widehat{p}_A \widehat{q}_B - \widehat{v}_{i,A} \widehat{f}_{i,B} - \widehat{q}_A \widehat{p}_B + \widehat{f}_{i,A} \widehat{v}_{i,B} \right) d^3\mathbf{x} \\ &= \oint_{\partial V^a} (\widehat{p}_A \widehat{v}_{i,B} - \widehat{v}_{i,A} \widehat{p}_B) n_i^a d^2\mathbf{x} + \oint_{\partial V^\cap} (\widehat{p}_A \widehat{v}_{i,B} - \widehat{v}_{i,A} \widehat{p}_B) n_i^a d^2\mathbf{x}, \end{aligned} \quad (1)$$

where $\widehat{p}(\mathbf{x}, \omega)$ and $\widehat{v}_i(\mathbf{x}, \omega)$ respectively represent the acoustic pressure and particle velocity with the A and B denoting two independent acoustic states; and $\widehat{f}_i(\mathbf{x}, \omega)$ and $\widehat{q}(\mathbf{x}, \omega)$ represent the source distributions in terms of external volume force density and volume injection rate density. Domain V^a represents an arbitrary acoustic spatial region enclosed by boundaries ∂V^a and ∂V^\cap with the outward-pointing normal vector $\mathbf{n}^a = n_i^a = [n_1^a, n_2^a, n_3^a]$, where a superscript a indicates a quantity defined in the acoustic medium. The boundary ∂V^\cap represents a coupled interface between the acoustic and elastic media (see Figure 1). Lowercase Latin subscripts take values of 1, 2, 3, and $\mathbf{x} = [x_1, x_2, x_3]$ denotes the Cartesian coordinate vector with the x_3 -axis oriented positive downward. Finally, note throughout that the summation convention applies for repeated subscripts, and a circumflex accent over a variable [e.g., $\widehat{p}(\mathbf{x}, \omega)$] indicates a Fourier transformed quantity in the frequency domain:

$$\widehat{p}(\mathbf{x}, \omega) = \int_{-\infty}^{\infty} p(\mathbf{x}, t) \exp(-j\omega t) dt, \quad (2)$$

where j is the imaginary unit and ω is angular frequency.

Equation 1 represents the acoustic reciprocity theorem of the convolution type, where frequency-domain products (e.g., $\widehat{p}_A \widehat{v}_{i,B}$) correspond to convolutions in the time domain. The field quantities in equation 1 – $\widehat{p}(\mathbf{x}, \omega)$, $\widehat{v}_i(\mathbf{x}, \omega)$, $\widehat{q}(\mathbf{x}, \omega)$, and $\widehat{f}_i(\mathbf{x}, \omega)$ – satisfy the space-frequency-domain acoustic

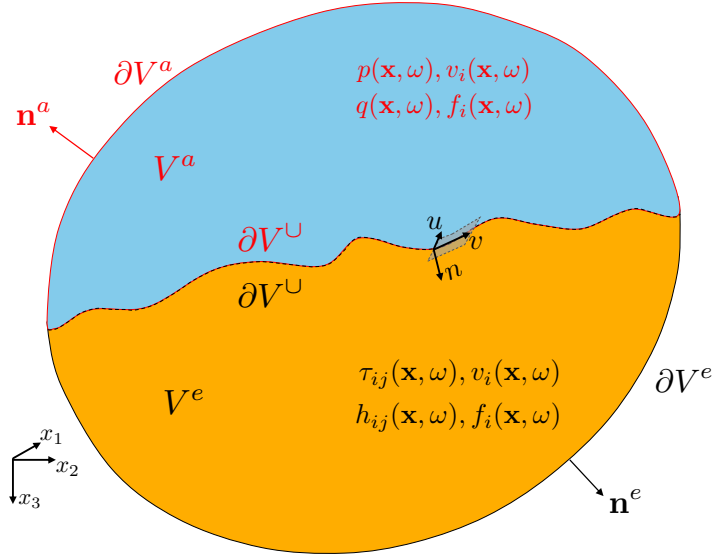


Figure 1. Configuration for a coupled acoustic (V^a)-elastic (V^e) system. The domains are coupled at common interface ∂V^\cap by the constitutive equations. The sources acting in V^a include the volume injection rate density q , and volume force density f_i while the observed wavefields are the pressure p and the particle velocity vector v_i . In V^e , the sources are the external deformation rate density h_{ij} and the external volume force density f_i , with the observed wavefields being the stress tensor τ_{ij} and the particle velocity vector v_i . The uv -plane shown is locally tangential to ∂V^\cap , with n as the normal vector.

114 wave equations representing a coupled first-order system in a lossless, arbitrarily inhomogeneous fluid
 115 medium:

$$j\omega\rho^a\hat{v}_i + \partial_i\hat{p} = \hat{f}_i \quad (3)$$

116 and

$$j\omega\kappa^a\hat{p} + \partial_i\hat{v}_i = \hat{q}, \quad (4)$$

117 where ∂_i denotes the partial derivative with respect to the x_i -direction; and $\rho^a = \rho^a(\mathbf{x})$ and $\kappa^a =$
 118 $\kappa^a(\mathbf{x})$ are the density and compressibility of the acoustic medium, respectively.

119 2.2 Elastic region

120 In elastic region V^e , we express the Rayleigh-Betti reciprocity theorem (Knopoff & Gangi 1959;
 121 De Hoop 1966; Aki & Richards 2002; Wapenaar & Fokkema 2006) as

$$\begin{aligned} & \int_{V^e} \left(-\hat{\tau}_{ij,A} \hat{h}_{ij,B} - \hat{v}_{i,A} \hat{f}_{i,B} + \hat{h}_{ij,A} \hat{\tau}_{ij,B} + \hat{f}_{i,A} \hat{v}_{i,B} \right) d^3\mathbf{x} \\ &= \oint_{\partial V^e} (\hat{v}_{i,A} \hat{\tau}_{ij,B} - \hat{\tau}_{ij,A} \hat{v}_{i,B}) n_j^e d^2\mathbf{x} + \oint_{\partial V^\cap} (\hat{v}_{i,A} \hat{\tau}_{ij,B} - \hat{\tau}_{ij,A} \hat{v}_{i,B}) n_j^e d^2\mathbf{x}, \end{aligned} \quad (5)$$

122 where $\tau_{ij}(\mathbf{x}, \omega)$ and $v_i(\mathbf{x}, \omega)$, respectively, are the components of the stress tensor and particle ve-
 123 locity vector with subscripts A and B again denoting two independent elastodynamic states; $f_i(\mathbf{x}, \omega)$
 124 denotes the external volume force density; and $h_{ij}(\mathbf{x}, \omega)$ represents the external deformation rate den-
 125 sity source types. Domain V^e represents an arbitrary elastic spatial region enclosed by boundaries
 126 ∂V^e and ∂V^\cap with an outward-pointing normal vector $\mathbf{n}^e = n_j^e = [n_1^e, n_2^e, n_3^e]$ where a superscript e
 127 denotes a quantity defined in the elastic solid. Boundary ∂V^\cap again represents the common coupled
 128 interface between acoustic and elastic domains ∂V^a and ∂V^e .

129 Equation 5 represents the elastodynamic reciprocity theorem of the convolution type. The associ-
 130 ated field quantities $-\widehat{\tau}_{ij}(\mathbf{x}, \omega)$, $\widehat{v}_i(\mathbf{x}, \omega)$, $\widehat{h}_{ij}(\mathbf{x}, \omega)$, and $\widehat{f}_i(\mathbf{x}, \omega)$ – satisfy the space-frequency domain
 131 elastic wave equations forming a coupled, first-order system in a lossless, arbitrarily inhomogeneous
 132 anisotropic elastic medium

$$\mathcal{J}\omega\rho^e\widehat{v}_i - \partial_j\widehat{\tau}_{ij} = \widehat{f}_i, \quad (6)$$

133 and

$$-\mathcal{J}\omega s_{ijkl}^e\widehat{\tau}_{kl} + \frac{1}{2}(\partial_i\widehat{v}_j + \partial_j\widehat{v}_i) = \widehat{h}_{ij}, \quad (7)$$

134 where $\rho^e = \rho^e(\mathbf{x})$ and $s_{ijkl}^e = s_{ijkl}^e(\mathbf{x})$ are the density and compliance of the elastic medium, respec-
 135 tively.

136 2.3 Interface boundary considerations

137 Applying the boundary conditions that couple the elastic and acoustic domains at the interface ∂V^\cap
 138 requires enforcing the continuity of traction and the normal component of the particle velocity. The
 139 continuity of traction at the acoustic-elastic interface ∂V^\cap is given by:

$$-\widehat{p} = \widehat{t}_n, \quad (8)$$

140 whereas

$$\widehat{t}_{nu} = \widehat{t}_{nv} = 0, \quad (9)$$

141 because an inviscid fluid cannot support shear stress. The continuity of the normal component of the
 142 particle velocity is expressed as

$$\widehat{v}_n^a = \widehat{v}_n^e. \quad (10)$$

143 In equations 8-10, \widehat{t}_n , \widehat{t}_{nu} , and \widehat{t}_{nv} represent the normal and shear tractions, while \widehat{v}_n^a and \widehat{v}_n^e are the
 144 normal particle velocity components in the acoustic and the elastic solid, respectively, at any point on
 145 ∂V^\cap . The normal vector n is relative to a locally orthogonal coordinate system, where the uv -plane

146 is locally tangential to that point on the interface ∂V^\cap (see Figure 1). The stresses and traction are
 147 related by $\hat{t}_i = \hat{\tau}_{ij} n_j$.

148 By virtue of equation 9, the reciprocity relation in equation 5 reduces to

$$\begin{aligned} & \int_{V^e} \left(-\hat{\tau}_{ij,A} \hat{h}_{ij,B} - \hat{v}_{i,A} \hat{f}_{i,B} + \hat{h}_{ij,A} \hat{\tau}_{ij,B} + \hat{f}_{i,A} \hat{v}_{i,B} \right) d^3 \mathbf{x} \\ &= \oint_{\partial V^e} (\hat{v}_{i,A} \hat{\tau}_{ij,B} - \hat{\tau}_{ij,A} \hat{v}_{i,B}) n_j^e d^2 \mathbf{x} + \oint_{\partial V^\cap} (\hat{v}_{n,A} \hat{t}_{n,B} - \hat{t}_{n,A} \hat{v}_{n,B}) d^2 \mathbf{x}. \end{aligned} \quad (11)$$

149 Using equations 8 and 10, and the fact that the normals defined on opposite sides of the interface ∂V^\cap
 150 must satisfy $\mathbf{n}^e = -\mathbf{n}^a$, we rewrite equation 11 as:

$$\begin{aligned} & \int_{V^a} \left(\hat{p}_A \hat{q}_B - \hat{v}_{i,A} \hat{f}_{i,B} - \hat{q}_A \hat{p}_B + \hat{f}_{i,A} \hat{v}_{i,B} \right) d^3 \mathbf{x} \\ &= \oint_{\partial V^a} (\hat{p}_A \hat{v}_{i,B} - \hat{v}_{i,A} \hat{p}_B) n_i^a d^2 \mathbf{x} - \oint_{\partial V^\cap} (\hat{v}_{n,A} \hat{t}_{n,B} - \hat{t}_{n,A} \hat{v}_{n,B}) d^2 \mathbf{x}. \end{aligned} \quad (12)$$

151 Adding equations 11 and 12 yields

$$\begin{aligned} & \int_{V^a} \left(\hat{p}_A \hat{q}_B - \hat{v}_{i,A} \hat{f}_{i,B} - \hat{q}_A \hat{p}_B + \hat{f}_{i,A} \hat{v}_{i,B} \right) d^3 \mathbf{x} \\ &+ \int_{V^e} \left(-\hat{\tau}_{ij,A} \hat{h}_{ij,B} - \hat{v}_{i,A} \hat{f}_{i,B} + \hat{h}_{ij,A} \hat{\tau}_{ij,B} + \hat{f}_{i,A} \hat{v}_{i,B} \right) d^3 \mathbf{x} \\ &= \oint_{\partial V^a} (\hat{p}_A \hat{v}_{i,B} - \hat{v}_{i,A} \hat{p}_B) n_i^a d^2 \mathbf{x} + \oint_{\partial V^e} (\hat{v}_{i,A} \hat{\tau}_{ij,B} - \hat{\tau}_{ij,A} \hat{v}_{i,B}) n_j^e d^2 \mathbf{x}. \end{aligned} \quad (13)$$

152 Equation 13 represents the convolution-type reciprocity for a coupled acoustic-elastic system, as
 153 frequency-domain products (e.g., $\hat{p}_A \hat{v}_{i,B}$) correspond to time-domain convolutions. A similar reci-
 154 procity relation to equation 13 is given in de Hoop (1990).

155 Because the acoustic and elastic media are assumed to be lossless, the principle of time-reversal
 156 invariance (Bojarski 1983) can be applied to both domains. In the frequency domain, time rever-
 157 sal is replaced by complex conjugation, which is denoted by the * symbol over the field quantities.
 158 Time-reversal invariance states that if \hat{p} and \hat{v}_i are solutions to the acoustic wave-equation system in
 159 equations 3 and 4 with source terms \hat{f}_i and \hat{q} , then \hat{p}^* and $-\hat{v}_i^*$ will satisfy the same equations with
 160 source terms \hat{f}_i^* and $-\hat{q}^*$. Similarly, when $\hat{\tau}_{ij}$ and \hat{v}_i are solutions to the elastic wave-equation system
 161 in equations 6 and 7 with source terms \hat{f}_i and \hat{h}_{ij} , then $\hat{\tau}_{ij}^*$ and $-\hat{v}_i^*$ will obey the same equations with
 162 source terms \hat{f}_i^* and $-\hat{h}_{ij}^*$.

163 Enforcing time reversal for state A in equation 13 leads to

$$\begin{aligned} & \int_{V^a} \left(\hat{p}_A^* \hat{q}_B + \hat{v}_{i,A}^* \hat{f}_{i,B} + \hat{q}_A^* \hat{p}_B + \hat{f}_{i,A}^* \hat{v}_{i,B} \right) d^3 \mathbf{x} \\ &+ \int_{V^e} \left(-\hat{\tau}_{ij,A}^* \hat{h}_{ij,B} + \hat{v}_{i,A}^* \hat{f}_{i,B} - \hat{h}_{ij,A}^* \hat{\tau}_{ij,B} + \hat{f}_{i,A}^* \hat{v}_{i,B} \right) d^3 \mathbf{x} \\ &= \oint_{\partial V^a} (\hat{p}_A^* \hat{v}_{i,B} + \hat{v}_{i,A}^* \hat{p}_B) n_i^a d^2 \mathbf{x} - \oint_{\partial V^e} (\hat{v}_{i,A}^* \hat{\tau}_{ij,B} + \hat{\tau}_{ij,A}^* \hat{v}_{i,B}) n_j^e d^2 \mathbf{x}. \end{aligned} \quad (14)$$

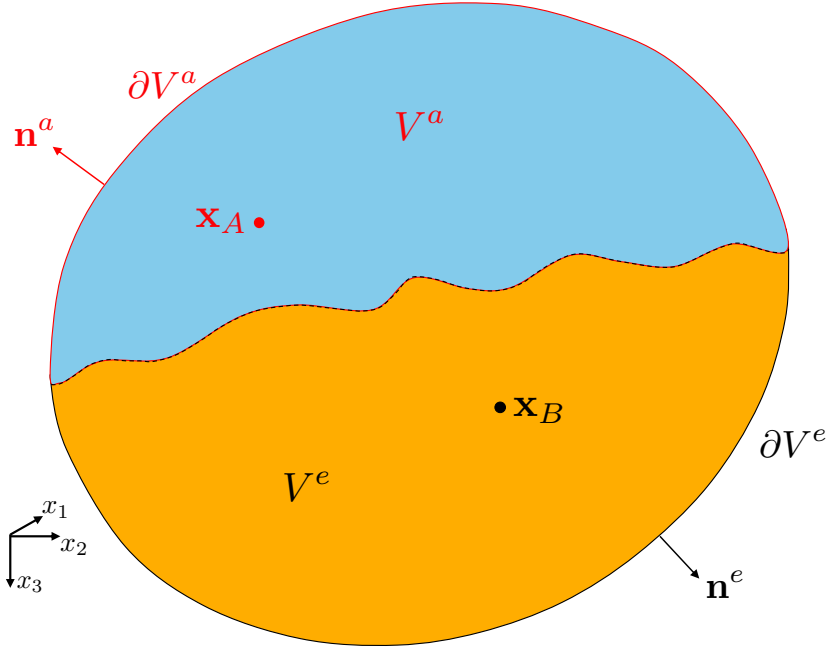


Figure 2. Configuration for coupled source-receiver reciprocity relations derived in Section 3.1. Points \mathbf{x}_A and \mathbf{x}_B are respectively located in the acoustic (V^a) and elastic (V^e) medium.

164 Equation 14 represents the correlation-type reciprocity for a coupled acoustic-elastic system, because
 165 frequency-domain products (e.g., $\widehat{p}_A^* \widehat{v}_{i,B}$) correspond to time-domain correlations. Finally, in both the
 166 coupled convolution and correlation-type reciprocity theorems above, the medium properties in states
 167 A and B are assumed to be identical.

168 3 COUPLED ACOUSTIC-ELASTIC DOMAIN'S GREEN'S FUNCTION 169 REPRESENTATIONS

170 In this section, we first derive the source-receiver reciprocity relations for the coupled acoustic-elastic
 171 system by substituting Green's functions for the wavefields in the convolution-type reciprocity re-
 172 lation (equation 13). We then derive the coupled-domain Green's function representations using the
 173 correlation-type reciprocity relation (equation 14). These representations form the foundation for SI
 174 in physically coupled acoustic-elastic systems, such as those found in exploration OBN settings. We
 175 consider a domain $V = V^a \cup V^e$ (see Figure 1). Boundaries ∂V^a and ∂V^e do not necessarily coincide
 176 with physical boundaries; however, they must be continuous on the ∂V^\cap interface.

177 3.1 Source-receiver reciprocity relations in coupled acoustic-elastic domain

178 We consider two cases involving two impulsive point sources: one located in the acoustic medium in
 179 state A , and the other in the solid in state B . In each case, \mathbf{x}_A is in the acoustic medium V^a and \mathbf{x}_B

Table 1. Summary of different source configurations in states A and B used in the coupled convolution-type reciprocity theorem for deriving coupled source-receiver reciprocity expressions.

Case	State A (\mathbf{x}_A in V^a)	State B (\mathbf{x}_B in V^e)
1	$\hat{q}_A = \delta(\mathbf{x} - \mathbf{x}_A)$, $\hat{f}_{i,A} = 0$	$\hat{h}_{ij,B} = 0$, $\hat{f}_{i,B} = \delta(\mathbf{x} - \mathbf{x}_B)\delta_{il}$
2	$\hat{q}_A = \delta(\mathbf{x} - \mathbf{x}_A)$, $\hat{f}_{i,A} = 0$	$\hat{h}_{ij,B} = \delta(\mathbf{x} - \mathbf{x}_B)\delta_{ir}\delta_{js}$, $\hat{f}_{i,B} = 0$

180 is in the solid medium V^e (see Figure 2). Table 1 summarizes these two cases and the chosen source
181 type.

182 Case 1 represents scenarios where only impulsive point sources of volume injection rate $\hat{q}(\mathbf{x}, \omega)$
183 at point \mathbf{x}_A in V^a in state A and impulsive point force sources $\hat{f}_i(\mathbf{x}, \omega)$ at point \mathbf{x}_B in V^e in state B
184 are present. In this case, the coupled convolution-type reciprocity relation (equation 13) simplifies to

$$\begin{aligned}
 & - \int_{V^a} \hat{q}_A \hat{p}_B d^3\mathbf{x} - \int_{V^e} \hat{v}_{i,A} \hat{f}_{i,B} d^3\mathbf{x} \\
 & = \oint_{\partial V^a} (\hat{p}_A \hat{v}_{i,B} - \hat{v}_{i,A} \hat{p}_B) n_i^a d^2\mathbf{x} + \oint_{\partial V^e} (\hat{v}_{i,A} \hat{\tau}_{ij,B} - \hat{\tau}_{ij,A} \hat{v}_{i,B}) n_j^e d^2\mathbf{x}.
 \end{aligned} \tag{15}$$

185 For an unbounded medium, we can consider the surface of integration ∂V^a and ∂V^e as a spherical
186 arc with infinite radius $r \rightarrow \infty$. In this case, the contributions from the boundary integrals over ∂V^a
187 and ∂V^e vanish, as they will be of order $O(r^{-1})$. Because the right-hand side of equation 15 vanishes
188 on both ∂V^a and ∂V^e , the result is independent of the specific choice of boundaries ∂V^a and ∂V^e ,
189 provided points \mathbf{x}_A and \mathbf{x}_B are contained within $\partial V^a \cup \partial V^e$. This further simplifies equation 15 to

$$\int_{V^a} \hat{q}_A \hat{p}_B d^3\mathbf{x} = - \int_{V^e} \hat{v}_{i,A} \hat{f}_{i,B} d^3\mathbf{x}. \tag{16}$$

190 Table 1 presents the Case 1 source definitions found in equation 16:

$$\hat{q}_A(\mathbf{x}, \omega) = \delta(\mathbf{x} - \mathbf{x}_A) \tag{17}$$

191 and

$$\hat{f}_{i,B}(\mathbf{x}, \omega) = \delta(\mathbf{x} - \mathbf{x}_B)\delta_{il}, \tag{18}$$

192 where $\delta(\mathbf{x})$ is the Dirac delta function and δ_{il} is the Kronecker delta function. The wavefields in states
193 A and B, needed in equation 16 due to above sources, can be expressed in terms of impulse responses
194 (i.e., acoustic and elastodynamic Green's functions):

$$\hat{p}_B(\mathbf{x}, \omega) = \hat{G}_i^{p,f}(\mathbf{x}, \mathbf{x}_B, \omega) \tag{19}$$

195 and

$$\hat{v}_{i,A}(\mathbf{x}, \omega) = \hat{G}_i^{v,q}(\mathbf{x}, \mathbf{x}_A, \omega). \tag{20}$$

196 Here, the Green's function notation $\widehat{G}_i^{v,q}(\mathbf{x}, \mathbf{x}_A, \omega)$ represents the impulse response observed at \mathbf{x} due
 197 to a source at \mathbf{x}_A . The double superscripts (v, q here) respectively represent the observed field quantity
 198 (here particle velocity v) and the applied source (here impulsive point sources of volume injection rate
 199 q). If the observed field quantity or source is a vector or tensor, its component or direction is indicated
 200 by the subscripts. In this case, subscript i denotes the i -th component of the observed particle velocity
 201 v . No subscript is required for scalar q quantities. A circumflex accent on \widehat{G} denotes the Fourier
 202 transform of causal time-domain Green's function $G_i^{v,q}(\mathbf{x}, \mathbf{x}_A, t)$.

203 Substituting equations 17-20 into equation 16 and using the sifting property of the delta function
 204 leads to a source-receiver reciprocity relation for the coupled acoustic-elastic system:

$$\widehat{G}_l^{p,f}(\mathbf{x}_A, \mathbf{x}_B, \omega) = -\widehat{G}_l^{v,q}(\mathbf{x}_B, \mathbf{x}_A, \omega). \quad (21)$$

205 Equation 21 represents the source-receiver reciprocity for an OBN acquisition scenario where the
 206 airgun sources or noise sources acting as a distributed pressure field are present anywhere above the
 207 seabed (i.e., in the water column), while the receivers are located just below the seabed (i.e., in the
 208 elastic solid).

209 Similarly, Case 2 is a scenario where we replace the source in equation 18 by a point impulsive
 210 source of external deformation rate density $\widehat{h}_{ij}(\mathbf{x}, \omega)$ defined as

$$\widehat{h}_{ij,B}(\mathbf{x}, \omega) = \delta(\mathbf{x} - \mathbf{x}_B) \delta_{ir} \delta_{js}, \quad (22)$$

211 where the other sources remain the same as Case 1. Table 1 presents this Case 2 source definitions.
 212 Here, the coupled convolution-type reciprocity relation (equation 13) simplifies to

$$\int_{V^a} \widehat{q}_A \widehat{p}_B d^3\mathbf{x} = - \int_{V^e} \widehat{\tau}_{ij,A} \widehat{h}_{ij,B} d^3\mathbf{x}. \quad (23)$$

213 We may express the wavefields needed in above the equation due to sources in Case 2 (Table 1) as

$$\widehat{p}_B(\mathbf{x}, \omega) = \widehat{G}_{rs}^{p,h}(\mathbf{x}, \mathbf{x}_B, \omega) \quad (24)$$

214 and

$$\widehat{\tau}_{ij,A}(\mathbf{x}, \omega) = \widehat{G}_{ij}^{\tau,q}(\mathbf{x}, \mathbf{x}_A, \omega). \quad (25)$$

215 Substituting equations 17, 22, 24 and 25 into equation 23 and using the sifting property of the
 216 delta function yields the following coupled source-receiver reciprocity relation

$$\widehat{G}_{rs}^{p,h}(\mathbf{x}_A, \mathbf{x}_B, \omega) = -\widehat{G}_{rs}^{\tau,q}(\mathbf{x}_B, \mathbf{x}_A, \omega). \quad (26)$$

217 For sources and receivers both located either in acoustic or elastic-solid media, the source-receiver
 218 reciprocity remains as presented in Wapenaar & Fokkema (2006). When both the source and receiver
 219 are in water and only impulsive point sources of volume injection rate q are acting in both states,

Table 2. Choice of sources and wavefields in V^a and V^e in states A and B, when points \mathbf{x}_A and \mathbf{x}_B are in V^a , to be used in the coupled convolution-type reciprocity theorem to derive pressure Green's function expression.

Domain	Parameter	State A	State B
in V^a	$\widehat{q}(\mathbf{x}, \omega)$	$\delta(\mathbf{x} - \mathbf{x}_A)$	$\delta(\mathbf{x} - \mathbf{x}_B)$
	$\widehat{f}_i(\mathbf{x}, \omega)$	0	0
	$\widehat{p}(\mathbf{x}, \omega)$	$\widehat{G}^{p,q}(\mathbf{x}, \mathbf{x}_A, \omega)$	$\widehat{G}^{p,q}(\mathbf{x}, \mathbf{x}_B, \omega)$
	$\widehat{v}_i(\mathbf{x}, \omega)$	$\frac{j}{\omega \rho^a(\mathbf{x})} \partial_i \widehat{G}^{p,q}(\mathbf{x}, \mathbf{x}_A, \omega)$	$\frac{j}{\omega \rho^a(\mathbf{x})} \partial_i \widehat{G}^{p,q}(\mathbf{x}, \mathbf{x}_B, \omega)$
in V^e	$\widehat{h}_{ij}(\mathbf{x}, \omega)$	0	0
	$\widehat{f}_i(\mathbf{x}, \omega)$	0	0
	$\widehat{\tau}_{ij}(\mathbf{x}, \omega)$	$\widehat{G}_{ij}^{\tau,q}(\mathbf{x}, \mathbf{x}_A, \omega)$	$\widehat{G}_{ij}^{\tau,q}(\mathbf{x}, \mathbf{x}_A, \omega)$
	$\widehat{v}_i(\mathbf{x}, \omega)$	$\widehat{G}_i^{v,q}(\mathbf{x}, \mathbf{x}_A, \omega)$	$\widehat{G}_i^{v,q}(\mathbf{x}, \mathbf{x}_B, \omega)$

reciprocity is given by

$$\widehat{G}^{p,q}(\mathbf{x}_B, \mathbf{x}_A, \omega) = \widehat{G}^{p,q}(\mathbf{x}_A, \mathbf{x}_B, \omega). \quad (27)$$

When both the source and receiver are in solid media, three scenarios must be addressed. First, for cases where impulsive point sources of force f are acting in both states, the reciprocity relation is

$$\widehat{G}_{m,n}^{v,f}(\mathbf{x}_B, \mathbf{x}_A, \omega) = \widehat{G}_{n,m}^{v,f}(\mathbf{x}_A, \mathbf{x}_B, \omega). \quad (28)$$

Second, when impulsive point sources of force f act in state A and point sources of deformation type h act in state B , the reciprocity relation

$$\widehat{G}_{qr,m}^{\tau,f}(\mathbf{x}_B, \mathbf{x}_A, \omega) = \widehat{G}_{m,qr}^{v,h}(\mathbf{x}_A, \mathbf{x}_B, \omega). \quad (29)$$

Third, when point sources of deformation type h are acting in both states, the reciprocity relation is

$$\widehat{G}_{qr,mn}^{\tau,h}(\mathbf{x}_B, \mathbf{x}_A, \omega) = \widehat{G}_{mn,qr}^{\tau,h}(\mathbf{x}_A, \mathbf{x}_B, \omega). \quad (30)$$

3.2 Pressure-type Green's function expression for seismic interferometry in coupled acoustic-elastic media

As with the coupled source-receiver reciprocity relations derived earlier, one can make specific choices regarding the wavefields and source fields in states A and B to derive the pressure Green's function representation for SI. In this section, we examine various cases for the locations of points \mathbf{x}_A and \mathbf{x}_B inside $\partial V^a \cup \partial V^e$ and define the corresponding sources and wavefields to derive the expression for the pressure-type Green's functions using the correlation-type coupled reciprocity relation derived in equation 14.

234 *3.2.1 Points \mathbf{x}_A and \mathbf{x}_B in acoustic media V^a*

235 For the scenario where points \mathbf{x}_A and \mathbf{x}_B are located in acoustic medium V^a , one need only consider
236 impulsive point sources of volume injection-rate density $\widehat{q}(\mathbf{x}, \omega)$ defined by

$$\widehat{q}_\chi(\mathbf{x}, \omega) = \delta(\mathbf{x} - \mathbf{x}_\chi) \quad \text{for } \chi = A, B, \quad (31)$$

237 while the external forces $\widehat{f}(\mathbf{x}, \omega)$ in V^a are assumed to be zero in both states. There are no sources
238 in V^e for states A and B . In this scenario, the correlation-type coupled reciprocity relation given in
239 equation 14 simplifies to

$$\begin{aligned} & \int_{V^a} (\widehat{p}_A^* \widehat{q}_B + \widehat{q}_A^* \widehat{p}_B) d^3\mathbf{x} \\ &= \oint_{\partial V^a} (\widehat{p}_A^* \widehat{v}_{i,B} + \widehat{v}_{i,A}^* \widehat{p}_B) n_i^a d^2\mathbf{x} - \oint_{\partial V^e} (\widehat{v}_{i,A}^* \widehat{\tau}_{ij,B} + \widehat{\tau}_{ij,A}^* \widehat{v}_{i,B}) n_j^e d^2\mathbf{x}. \end{aligned} \quad (32)$$

240 We define the recorded pressure wavefield $\widehat{p}(\mathbf{x}, \omega)$ at \mathbf{x} in V^a for both the states as the observed
241 impulse responses (Green's functions), given by:

$$\widehat{p}_\chi(\mathbf{x}, \omega) = \widehat{G}^{p,q}(\mathbf{x}, \mathbf{x}_\chi, \omega) \quad \text{for } \chi = A, B. \quad (33)$$

242 We then obtain the expressions for the particle velocities observed at \mathbf{x} in V^a for both the states by
243 substituting equation 33 and $\widehat{f}_A(\mathbf{x}, \omega) = \widehat{f}_B(\mathbf{x}, \omega) = 0$ into the acoustic wave equation 3 as:

$$\widehat{v}_{i,\chi}(\mathbf{x}, \omega) = \frac{-1}{j\omega\rho^a(\mathbf{x})} \partial_i \widehat{G}^{p,q}(\mathbf{x}, \mathbf{x}_\chi, \omega) \quad \text{for } \chi = A, B. \quad (34)$$

244 For the stress and velocity wavefields recorded at \mathbf{x} in V^e for both states, we define the stress and
245 velocity Green's functions due to the sources in equations 31 as

$$\widehat{\tau}_{ij,\chi}(\mathbf{x}, \omega) = \widehat{G}_{ij}^{\tau,q}(\mathbf{x}, \mathbf{x}_\chi, \omega) \quad \text{for } \chi = A, B, \quad (35)$$

246 and

$$\widehat{v}_{i,\chi}(\mathbf{x}, \omega) = \widehat{G}_i^{v,q}(\mathbf{x}, \mathbf{x}_\chi, \omega) \quad \text{for } \chi = A, B. \quad (36)$$

247 Table 2 summarizes the sources along with the corresponding wavefields in V^a and V^e for both states.

248 Substituting equations 31, 33-36 into equation 32 and applying the sifting property of the Dirac
249 delta function obtains

$$\begin{aligned} & \widehat{G}^{p,q*}(\mathbf{x}_B, \mathbf{x}_A, \omega) + \widehat{G}^{p,q}(\mathbf{x}_A, \mathbf{x}_B, \omega) \\ &= \oint_{\partial V^a} \frac{-1}{j\omega\rho^a(\mathbf{x})} \left(\widehat{G}^{p,q*}(\mathbf{x}, \mathbf{x}_A, \omega) \partial_i \widehat{G}^{p,q}(\mathbf{x}, \mathbf{x}_B, \omega) - \partial_i \widehat{G}^{p,q*}(\mathbf{x}, \mathbf{x}_A, \omega) \widehat{G}^{p,q}(\mathbf{x}, \mathbf{x}_B, \omega) \right) n_i^a d^2\mathbf{x} \\ & \quad - \oint_{\partial V^e} \left(\widehat{G}_i^{v,q*}(\mathbf{x}, \mathbf{x}_A, \omega) \widehat{G}_{ij}^{\tau,q}(\mathbf{x}, \mathbf{x}_B, \omega) + \widehat{G}_{ij}^{\tau,q*}(\mathbf{x}, \mathbf{x}_A, \omega) \widehat{G}_i^{v,q}(\mathbf{x}, \mathbf{x}_B, \omega) \right) n_j^e d^2\mathbf{x}. \end{aligned} \quad (37)$$

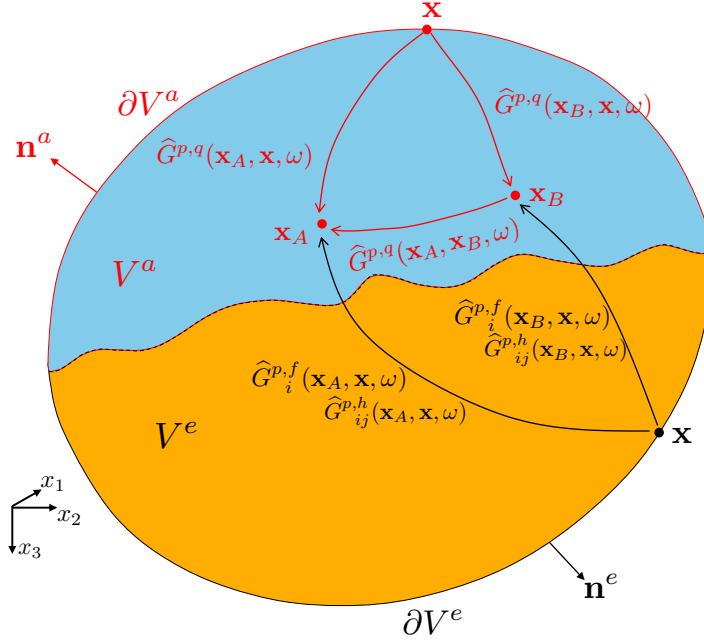


Figure 3. Seismic interferometry by cross-correlation for the pressure-type Green's function representation when receivers are in V^a . Green's function $\hat{G}^{p,q}(\mathbf{x}_A, \mathbf{x}_B, \omega)$ can be obtained by cross-correlating the observations at \mathbf{x}_A and \mathbf{x}_B , and integrating along the source coordinate \mathbf{x} at ∂V^a and ∂V^e (equation 38). The figure shows the wavefields observed at \mathbf{x}_A and \mathbf{x}_B along with the corresponding sources required at \mathbf{x} on ∂V^a and ∂V^e for pressure Green's function retrieval. Note that the rays represent the full responses between the source and receiver points, including primary and multiple scattering mode conversions due to inhomogeneities inside and outside the region $\partial V^a \cup \partial V^e$.

250 Applying source-receiver reciprocity from equations 21-27 into both sides of the above results in

$$\begin{aligned}
 & 2 \Re \left\{ \hat{G}^{p,q}(\mathbf{x}_A, \mathbf{x}_B, \omega) \right\} \\
 = & \oint_{\partial V^a} \frac{-1}{j\omega\rho^a(\mathbf{x})} \left(\hat{G}^{p,q*}(\mathbf{x}_A, \mathbf{x}, \omega) \partial_i \hat{G}^{p,q}(\mathbf{x}_B, \mathbf{x}, \omega) - \partial_i \hat{G}^{p,q*}(\mathbf{x}_A, \mathbf{x}, \omega) \hat{G}^{p,q}(\mathbf{x}_B, \mathbf{x}, \omega) \right) n_i^a d^2\mathbf{x} \\
 & - \oint_{\partial V^e} \left(\hat{G}_i^{p,f*}(\mathbf{x}_A, \mathbf{x}, \omega) \hat{G}_{ij}^{p,h}(\mathbf{x}_B, \mathbf{x}, \omega) + (\hat{G}_{ij}^{p,h*}(\mathbf{x}_A, \mathbf{x}, \omega) \hat{G}_i^{p,f}(\mathbf{x}_B, \mathbf{x}, \omega)) \right) n_j^e d^2\mathbf{x}.
 \end{aligned} \tag{38}$$

251 where the \Re operator extracts the real part of a complex argument.

252 In the time domain, the products on the right-hand side of the above equation (e.g., $\hat{G}^{p,q*} \partial_i \hat{G}^{p,q}$)
 253 correspond to cross correlations, while the left-hand side represents the pressure Green's function
 254 and its time-reversed counterpart [i.e., $G^{p,q}(\mathbf{x}_A, \mathbf{x}_B, t) + G^{p,q}(\mathbf{x}_A, \mathbf{x}_B, -t)$]. The term $\hat{G}^{p,q}$ under
 255 the acoustic-surface integral $\oint_{\partial V^a}$ denotes the response of the volume injection-rate density sources
 256 q at \mathbf{x} on ∂V^a . Similarly, the terms $\hat{G}_i^{p,f}$ and $\hat{G}_{ij}^{p,h}$ under the solid-surface integral $\oint_{\partial V^e}$ respectively
 257 represent the responses of force sources f and deformation sources h at \mathbf{x} on ∂V^e . Integration in both
 258 integrals is performed along the source coordinate \mathbf{x} (see Figure 3).

259 The exact relationship expressed in equation 38 provides a means to retrieve the complete pres-
 260 sure Green's function $\widehat{G}^{p,q}(\mathbf{x}_A, \mathbf{x}_B, \omega)$ using cross correlations of observed Green's functions from
 261 sources on ∂V^a and ∂V^e (Figure 3). This formulation applies to any lossless, arbitrary, inhomogeneous,
 262 anisotropic, coupled acoustic-elastic medium and forms the basis for acoustic SI when receivers
 263 are located within the acoustic medium. The retrieved Green's function is complete, containing
 264 all arrivals—direct and scattered—including primaries, multiples, and mode conversions from inhomogeneities
 265 both within and outside the boundaries ∂V^a and ∂V^e .

266 Although equation 38 is an exact representation of the acoustic Green's function, it is impractical
 267 for field data applications in its current form due to its complexity. Specifically, one must evaluate the
 268 superposition of two correlation products under both integrals, $\oint_{\partial V^a}$ and $\oint_{\partial V^e}$. Furthermore, monopole
 269 $\widehat{G}^{p,q}$ as well as dipole responses $\partial_i \widehat{G}^{p,q}$ are required for all source positions \mathbf{x} on V^a . Similarly, two
 270 different types of sources, $\widehat{f}(\mathbf{x}, \omega)$ and $\widehat{h}(\mathbf{x}, \omega)$, are required for all source positions \mathbf{x} on V^e . To
 271 overcome these challenges, we develop practical approximations for both integrals.

272 ***Simplification of the acoustic boundary integral (equation 37):*** When the wavefield on the bound-
 273 ary ∂V^a satisfies outgoing (i.e., radiation or absorbing) boundary conditions such that the outward-
 274 propagating wavefield at the ∂V^a boundary does not return after being scattered by external inhomogeneities
 275 ∂V^a , Wapenaar & Fokkema (2006) demonstrates that the acoustic boundary integral can be
 276 approximated as:

$$\text{Acoustic Boundary Integral} \approx \frac{2}{\rho^a c^a} \oint_{\partial V^a} \widehat{G}^{p,q*}(\mathbf{x}_A, \mathbf{x}, \omega) \widehat{G}^{p,q}(\mathbf{x}_B, \mathbf{x}, \omega) d^2\mathbf{x}, \quad (39)$$

277 where the acoustic medium at and outside ∂V^a is assumed to be homogeneous with a propagation
 278 velocity c^a and mass density ρ^a .

279 ***Simplification of the elastic boundary integrand (equation 37):*** To approximate the contribution
 280 of sources on the elastic boundary ∂V^e to the acoustic Green's function $2 \Re\{\widehat{G}^{p,q}(\mathbf{x}_A, \mathbf{x}_B, \omega)\}$ in
 281 equation 37, we can follow the procedure developed in Wapenaar & Fokkema (2006) starting with
 282 equation A-9 found therein. This simplification involves decomposing the wavefield under the domain
 283 boundary integrand into inward- and outward-propagating components and assuming that the medium
 284 outside the domain is isotropic and homogeneous, ensuring the absence of cross-terms between inward
 285 and outward propagating waves. The complete argument is thoroughly developed in Wapenaar &
 286 Haimé (1990). Accordingly, we assume the solid medium at and outside ∂V^e to be homogeneous,
 287 isotropic, and source-free, with mass density ρ^e , and P- and S-wave velocities c_P and c_S . The elastic
 288 boundary integral term in the convolution-type reciprocity relation (equation 14) can then be expressed
 289 as (see equation A-9 in Wapenaar & Fokkema (2006)):

$$- \oint_{\partial V^e} (\widehat{v}_{i,A}^* \widehat{\tau}_{ij,B} + \widehat{\tau}_{ij,A}^* \widehat{v}_{i,B}) n_j^e d^2\mathbf{x} \approx \frac{2}{j\omega\rho^e} \oint_{\partial V^e} \left((\partial_j \widehat{\Phi}_A^*) \widehat{\Phi}_B + (\partial_j \widehat{\Psi}_{k,A}^*) \widehat{\Psi}_{k,B} \right) n_j^e d^2\mathbf{x}, \quad (40)$$

290 where $\widehat{\Phi}$ and $\widehat{\Psi}_k$ respectively represent the observed P- and S-wave potentials at \mathbf{x} on ∂V^e with
 291 subscripts A and B correspond to states A and B . These potentials satisfy the Helmholtz equations
 292 (Aki & Richards 2002).

293 In the current case (Case 1 in Table 2), points \mathbf{x}_A and \mathbf{x}_B are located above the seafloor, and we
 294 have chosen impulsive point sources with volume injection-rate density $\widehat{q}(\mathbf{x}, \omega)$ at points \mathbf{x}_A in state
 295 A and at \mathbf{x}_B in state B . For \mathbf{x} in V^e , the velocity and stresses in both the states due to above sources
 296 at \mathbf{x}_A and \mathbf{x}_B are expressed in terms of coupled Green's functions as given in equations 35 and 36.
 297 For \mathbf{x} at or outside ∂V^e but still in solid, we express the P- and S-wave potentials in states A and B in
 298 terms of Green's functions as

$$\widehat{\Phi}_\chi(\mathbf{x}, \omega) = \widehat{G}_0^{\phi, q}(\mathbf{x}, \mathbf{x}_\chi, \omega) \quad \text{for } \chi = A, B \quad (41)$$

299 and

$$\widehat{\Psi}_{k, \chi}(\mathbf{x}, \omega) = \widehat{G}_k^{\phi, q}(\mathbf{x}, \mathbf{x}_\chi, \omega) \quad \text{for } \chi = A, B, \quad (42)$$

300 where the superscript ϕ denotes that the observed wavefield quantity at \mathbf{x} is a P- or S-wave potential.
 301 To describe both wave types with a single Green's function, we use subscript K that takes on values 0,
 302 1, 2, and 3. Hence, in $\widehat{G}_K^{\phi, q}(\mathbf{x}, \mathbf{x}_B, \omega)$, the observed wavefield at \mathbf{x} is a P wave for $K = 0$ or an S-wave
 303 component for $K = k = 1, 2, 3$. Substituting equations 35, 36, 41 and 42 into equation 40 gives

$$\begin{aligned} & - \oint_{\partial V^e} \left(\widehat{G}_i^{v, q*}(\mathbf{x}, \mathbf{x}_A, \omega) \widehat{G}_{ij}^{\tau, q}(\mathbf{x}, \mathbf{x}_B, \omega) + \widehat{G}_{ij}^{\tau, q*}(\mathbf{x}, \mathbf{x}_A, \omega) \widehat{G}_i^{v, q}(\mathbf{x}, \mathbf{x}_B, \omega) \right) n_j^e d^2 \mathbf{x} \\ & \approx \frac{2}{j\omega\rho^e} \oint_{\partial V^e} \partial_j \widehat{G}_K^{\phi, q*}(\mathbf{x}, \mathbf{x}_A, \omega) \widehat{G}_K^{\phi, q}(\mathbf{x}, \mathbf{x}_B, \omega) n_j^e d^2 \mathbf{x}. \end{aligned} \quad (43)$$

304 Note that the repeated subscript K now represents a summation from 0 to 3, accounting for the dif-
 305 ferent wave types in equation 40, and that the left-hand side is the elastic boundary integral from
 306 equation 37. Let us examine the source-receiver reciprocity for the Green's function $\widehat{G}_K^{\phi, q}(\mathbf{x}, \mathbf{x}_A, \omega)$,
 307 where \mathbf{x} lies in the solid and \mathbf{x}_A is in the water. In this case (refer to Table 1, Case 1 for the source
 308 configuration), we can write the source-receiver reciprocity relation (equation 21) as

$$\widehat{G}_i^{p, f}(\mathbf{x}_A, \mathbf{x}, \omega) = -\widehat{G}_i^{v, q}(\mathbf{x}, \mathbf{x}_A, \omega). \quad (44)$$

309 Alternatively, if the source $\widehat{f}(\mathbf{x}, \omega)$ is replaced with impulsive P- and S-wave point sources (Wapenaar
 310 & Berkhout 1989) at \mathbf{x} , we can define another coupled source-receiver reciprocity as:

$$\widehat{G}_K^{p, \phi}(\mathbf{x}_A, \mathbf{x}, \omega) = -\widehat{G}_K^{\phi, q}(\mathbf{x}, \mathbf{x}_A, \omega). \quad (45)$$

311 In this case, the superscript ϕ in $\widehat{G}_K^{p, \phi}(\mathbf{x}_A, \mathbf{x}, \omega)$ indicates a P-wave source for $K = 0$ or a vector-
 312 polarized S-wave source for $K = k = 1, 2, 3$. Accordingly, in $\widehat{G}_K^{\phi, q}(\mathbf{x}, \mathbf{x}_A, \omega)$, the observed wave
 313 potential at \mathbf{x} is the P-wave potential for $K = 0$, and the S-wave potential for $K = k = 1, 2, 3$.

314 Introducing the above reciprocity relation in equation 43 results in

$$\text{Elastic Boundary Integral} \approx \frac{2}{j\omega\rho^e} \oint_{\partial V^e} \partial_j \widehat{G}_K^{p,\phi*}(\mathbf{x}_A, \mathbf{x}, \omega) \widehat{G}_K^{p,\phi}(\mathbf{x}_B, \mathbf{x}, \omega) n_j^e d^2\mathbf{x}. \quad (46)$$

315 Despite its simple form, the above equation requires the availability of monopole and dipole responses,
 316 $\widehat{G}^{p,\phi}$ and $\partial_i \widehat{G}_K^{p,\phi}$, from P- and S-wave sources at \mathbf{x} . Assuming as previously that the solid medium at
 317 and outside ∂V^e is homogeneous with mass density ρ^e and P- and S-wave velocities c^P and c^S ,
 318 respectively, the dipole response can be approximated in terms of a monopole response (Wapenaar &
 319 Fokkema 2006) as

$$\partial_j \widehat{G}_K^{p,\phi}(\mathbf{x}_A, \mathbf{x}, \omega) n_j^e \approx \frac{\omega}{jc^K} \widehat{G}_K^{p,\phi}(\mathbf{x}_A, \mathbf{x}, \omega), \quad (47)$$

320 where

$$c^K = \begin{cases} c^P & \text{for } K = 0 \\ c^S & \text{for } K = k = 1, 2, 3. \end{cases} \quad (48)$$

321 Note that since K does not appear as a subscript in c^K , no summation takes place over K on the
 322 right-hand side of equation 47. Using the dipole approximation from equation 47 in equation 46, the
 323 elastic boundary integral reduces to:

$$\text{Elastic Boundary Integral} \approx \frac{2}{\rho^e c^K} \oint_{\partial V^e} \widehat{G}_K^{p,\phi*}(\mathbf{x}_A, \mathbf{x}, \omega) \widehat{G}_K^{p,\phi}(\mathbf{x}_B, \mathbf{x}, \omega) d^2\mathbf{x}. \quad (49)$$

324 Using the acoustic and elastic boundary integral approximations (equations 39 and 49), the pressure
 325 Green's function in equation 37 approximates to:

$$\begin{aligned} & \Re \left\{ \widehat{G}^{p,q}(\mathbf{x}_A, \mathbf{x}_B, \omega) \right\} \\ & \approx \frac{1}{\rho^a c^a} \oint_{\partial V^a} \widehat{G}^{p,q*}(\mathbf{x}_A, \mathbf{x}, \omega) \widehat{G}^{p,q}(\mathbf{x}_B, \mathbf{x}, \omega) d^2\mathbf{x} \\ & + \frac{1}{\rho^e c^K} \oint_{\partial V^e} \widehat{G}_K^{p,\phi*}(\mathbf{x}_A, \mathbf{x}, \omega) \widehat{G}_K^{p,\phi}(\mathbf{x}_B, \mathbf{x}, \omega) d^2\mathbf{x}. \end{aligned} \quad (50)$$

326 This approximation is highly accurate when ∂V^a and ∂V^e are part of a sphere with a sufficiently large
 327 radius such that all rays are normal to ∂V^a and ∂V^e ; otherwise, it may introduce significant amplitude
 328 errors. Additionally, events that would be otherwise completely cancelled when using equation 38 may
 329 instead give rise to artifacts due to incomplete destructive interference. Nonetheless, the application
 330 of equation 50 will correctly retrieve the phases of all arrivals.

331 3.2.2 Points \mathbf{x}_A and \mathbf{x}_B in the solid media V^e

332 When both points are located beneath the seafloor, we place impulsive point sources of the external
 333 deformation rate density $\widehat{h}_{ij}(\mathbf{x}, \omega)$ at \mathbf{x}_A and \mathbf{x}_B within V^e , with all other sources set to zero. Table 3
 334 summarizes these sources and the resulting wavefields in both V^a and V^e for the two states. Substitut-

Table 3. Summary of sources and wavefields in states A and B , used for the pressure Green's function expression when points \mathbf{x}_A and \mathbf{x}_B are in V^e .

Domain	Parameter	State A	State B
in V^a	$\hat{q}(\mathbf{x}, \omega)$	0	0
	$\hat{f}_i(\mathbf{x}, \omega)$	0	0
	$\hat{p}(\mathbf{x}, \omega)$	$\hat{G}_{mm}^{p,h}(\mathbf{x}, \mathbf{x}_A, \omega)$	$\hat{G}_{rr}^{p,h}(\mathbf{x}, \mathbf{x}_B, \omega)$
	$\hat{v}_i(\mathbf{x}, \omega)$	$\frac{j}{\omega\rho^a(\mathbf{x})}\partial_i\hat{G}_{mm}^{p,h}(\mathbf{x}, \mathbf{x}_A, \omega)$	$\frac{j}{\omega\rho^a(\mathbf{x})}\partial_i\hat{G}_{rr}^{p,h}(\mathbf{x}, \mathbf{x}_B, \omega)$
in V^e	$\hat{h}_{ii}(\mathbf{x}, \omega)$	$\delta(\mathbf{x} - \mathbf{x}_A)\delta_{im}$	$\delta(\mathbf{x} - \mathbf{x}_B)\delta_{ir}$
	$\hat{f}_i(\mathbf{x}, \omega)$	0	0
	$\hat{\tau}_{ij}(\mathbf{x}, \omega)$	$\hat{G}_{ij,mm}^{\tau,h}(\mathbf{x}, \mathbf{x}_A, \omega)$	$\hat{G}_{ij,rr}^{\tau,h}(\mathbf{x}, \mathbf{x}_B, \omega)$
	$\hat{v}_i(\mathbf{x}, \omega)$	$\hat{G}_{i,mm}^{v,h}(\mathbf{x}, \mathbf{x}_A, \omega)$	$\hat{G}_{i,rr}^{\tau,h}(\mathbf{x}, \mathbf{x}_B, \omega)$

335 ing the parameters from Table 3 into the reciprocity relation in equation 14 and using the Dirac delta
 336 function sifting property yields:

$$\begin{aligned}
 & \left(\hat{G}_{rr,mm}^{\tau,h*}(\mathbf{x}_B, \mathbf{x}_A, \omega) + \hat{G}_{mm,rr}^{\tau,h}(\mathbf{x}_A, \mathbf{x}_B, \omega) \right) \\
 = & \oint_{\partial V^a} \frac{1}{j\omega\rho^a(\mathbf{x})} \left(\hat{G}_{mm}^{p,h*}(\mathbf{x}, \mathbf{x}_A, \omega) \partial_i \hat{G}_{rr}^{p,h}(\mathbf{x}, \mathbf{x}_B, \omega) - \partial_i \hat{G}_{mm}^{p,h*}(\mathbf{x}, \mathbf{x}_A, \omega) \hat{G}_{rr}^{p,h}(\mathbf{x}, \mathbf{x}_B, \omega) \right) n_i^a d^2\mathbf{x} \\
 & + \oint_{\partial V^e} \left(\hat{G}_{i,mm}^{v,h*}(\mathbf{x}, \mathbf{x}_A, \omega) \hat{G}_{ij,rr}^{\tau,h}(\mathbf{x}, \mathbf{x}_B, \omega) + \hat{G}_{ij,mm}^{\tau,h*}(\mathbf{x}, \mathbf{x}_A, \omega) \hat{G}_{i,rr}^{v,h}(\mathbf{x}, \mathbf{x}_B, \omega) \right) n_j^e d^2\mathbf{x}.
 \end{aligned} \tag{51}$$

337 Using the source-receiver reciprocity of equations 26, 29 and 30 into the above equation results in

$$\begin{aligned}
 & 2 \Re \left\{ \hat{G}_{mm,rr}^{\tau,h}(\mathbf{x}_A, \mathbf{x}_B, \omega) \right\} \\
 = & \oint_{\partial V^a} \frac{1}{x_j\omega\rho^a(\mathbf{x})} \left(\hat{G}_{mm}^{\tau,q*}(\mathbf{x}_A, \mathbf{x}, \omega) \partial_i \hat{G}_{rr}^{\tau,q}(\mathbf{x}_B, \mathbf{x}, \omega) - \partial_i \hat{G}_{mm}^{\tau,q*}(\mathbf{x}_A, \mathbf{x}, \omega) \hat{G}_{rr}^{\tau,q}(\mathbf{x}_B, \mathbf{x}, \omega) \right) n_i^a d^2\mathbf{x} \\
 & + \oint_{\partial V^e} \left(\hat{G}_{mm,i}^{\tau,f*}(\mathbf{x}_A, \mathbf{x}, \omega) \hat{G}_{rr,ij}^{\tau,h}(\mathbf{x}_B, \mathbf{x}, \omega) + \hat{G}_{mm,ij}^{\tau,h*}(\mathbf{x}_A, \mathbf{x}, \omega) \hat{G}_{rr,i}^{\tau,f}(\mathbf{x}_B, \mathbf{x}, \omega) \right) n_j^e d^2\mathbf{x}.
 \end{aligned} \tag{52}$$

338 Assuming an isotropic elastic solid, we define pressure as the stress tensor trace (Bennethum 2006)

$$\hat{p}^e = -\frac{1}{3}(\hat{\tau}_{11} + \hat{\tau}_{22} + \hat{\tau}_{33}). \tag{53}$$

339 Because the sources are impulsive point stress sources, we write the above pressure equation as

$$\begin{aligned}
 \hat{p}^e = -\hat{G}^{\tau tr, htr} & = -\frac{1}{3} \left(\hat{G}_{11}^{\tau, htr} + \hat{G}_{22}^{\tau, htr} + \hat{G}_{33}^{\tau, htr} \right) \\
 & = -\frac{1}{9} \left((\hat{G}_{11,11}^{\tau, h} + \hat{G}_{11,22}^{\tau, h} + \hat{G}_{11,33}^{\tau, h}) \right. \\
 & \quad + (\hat{G}_{22,11}^{\tau, h} + \hat{G}_{22,22}^{\tau, h} + \hat{G}_{22,33}^{\tau, h}) \\
 & \quad \left. + (\hat{G}_{33,11}^{\tau, h} + \hat{G}_{33,22}^{\tau, h} + \hat{G}_{33,33}^{\tau, h}) \right)
 \end{aligned} \tag{54}$$

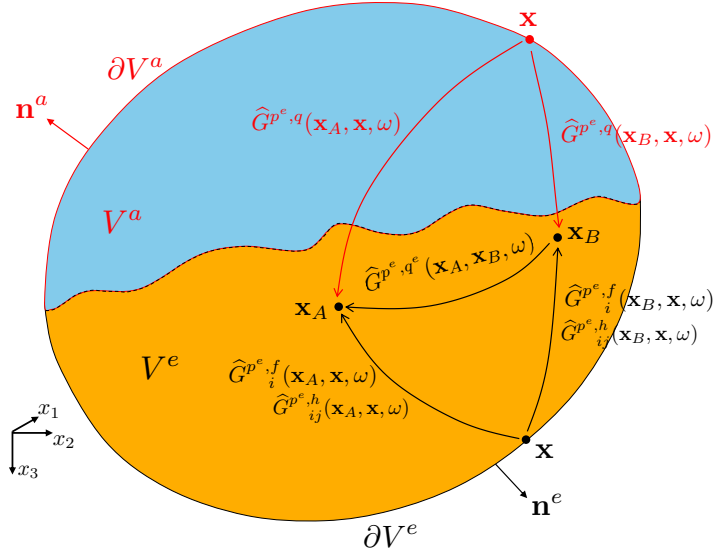


Figure 4. Pressure-type Green's function representation through interferometry when both the receivers are in V^e . According to equation 56, the Green's function $\widehat{G}^{p^e, q^e}(\mathbf{x}_A, \mathbf{x}_B, \omega)$ can be obtained by cross-correlating the observations at \mathbf{x}_A and \mathbf{x}_B , and integrating along the source coordinate \mathbf{x} at ∂V^a and ∂V^e . The wavefields observed at \mathbf{x}_A and \mathbf{x}_B , along with the corresponding sources required at \mathbf{x} on ∂V^a and ∂V^e for Green's function $\widehat{G}^{p^e, q^e}(\mathbf{x}_A, \mathbf{x}_B, \omega)$ retrieval, are shown. Note that the rays in this figure represent the full responses between the source and receiver points, including primary and multiple scattering, as well as mode conversion due to inhomogeneities inside and outside the region $\partial V^a \cup \partial V^e$.

340 due to a corresponding composite source of volume injection type

$$\widehat{q}^e = \widehat{h}_{tr} = \frac{1}{3} (\widehat{h}_{11} + \widehat{h}_{22} + \widehat{h}_{33}). \quad (55)$$

341 Using these definitions and applying the summation convention, we rewrite equation 52 as:

$$\begin{aligned} & 2 \Re \left\{ \widehat{G}^{p^e, q^e}(\mathbf{x}_A, \mathbf{x}_B, \omega) \right\} \\ &= \oint_{\partial V^a} \frac{-1}{j\omega\rho^a(\mathbf{x})} \left(\widehat{G}^{p^e, q^*}(\mathbf{x}_A, \mathbf{x}, \omega) \partial_i \widehat{G}^{p^e, q}(\mathbf{x}_B, \mathbf{x}, \omega) - \partial_i \widehat{G}^{p^e, q^*}(\mathbf{x}_A, \mathbf{x}, \omega) \widehat{G}^{p^e, q}(\mathbf{x}_B, \mathbf{x}, \omega) \right) n_i^a d^2\mathbf{x} \\ & \quad - \oint_{\partial V^e} \left(\widehat{G}^{p^e, f^*}(\mathbf{x}_A, \mathbf{x}, \omega) \widehat{G}^{p^e, h}(\mathbf{x}_B, \mathbf{x}, \omega) + \widehat{G}^{p^e, h^*}(\mathbf{x}_A, \mathbf{x}, \omega) \widehat{G}^{p^e, f}(\mathbf{x}_B, \mathbf{x}, \omega) \right) n_j^e d^2\mathbf{x}. \end{aligned} \quad (56)$$

342 Figure 4 illustrates the Green's functions of the above equation observed at \mathbf{x}_A and \mathbf{x}_B and corre-
343 sponding sources required at \mathbf{x} on ∂V^a and ∂V^e to obtain the Green's function $\widehat{G}^{p^e, q^e}(\mathbf{x}_A, \mathbf{x}_B, \omega)$.

344 Equation 56 is identical to equation 38, except that \widehat{p}^e and \widehat{q}^e in this context are defined for the
345 elastodynamic state. Consequently, it can be approximated using a similar expression to equation 50:

$$\begin{aligned} \Re \left\{ \widehat{G}^{p^e, q^e}(\mathbf{x}_A, \mathbf{x}_B, \omega) \right\} &\approx \frac{1}{\rho^a c^a} \oint_{\partial V^a} \widehat{G}^{p^e, q^*}(\mathbf{x}_A, \mathbf{x}, \omega) \widehat{G}^{p^e, q}(\mathbf{x}_B, \mathbf{x}, \omega) d^2\mathbf{x} \\ & \quad + \frac{1}{\rho^e c^K} \oint_{\partial V^e} \widehat{G}^{p^e, \phi^*}_K(\mathbf{x}_A, \mathbf{x}, \omega) \widehat{G}^{p^e, \phi}_K(\mathbf{x}_B, \mathbf{x}, \omega) d^2\mathbf{x}, \end{aligned} \quad (57)$$

Table 4. Summary of sources and wavefields in states A and B , used for the pressure Green's function expression when point \mathbf{x}_A is in V^a , and point \mathbf{x}_B is in V^e .

Domain	Parameter	State A	State B
in V^a	$\hat{q}(\mathbf{x}, \omega)$	$\delta(\mathbf{x} - \mathbf{x}_A)$	0
	$\hat{f}_i(\mathbf{x}, \omega)$	0	0
	$\hat{p}(\mathbf{x}, \omega)$	$\hat{G}^{p,q}(\mathbf{x}, \mathbf{x}_A, \omega)$	$\hat{G}_{rr}^{p,h}(\mathbf{x}, \mathbf{x}_B, \omega)$
	$\hat{v}_i(\mathbf{x}, \omega)$	$\frac{j}{\omega\rho^a(\mathbf{x})}\partial_i\hat{G}^{p,q}(\mathbf{x}, \mathbf{x}_A, \omega)$	$\frac{j}{\omega\rho^a(\mathbf{x})}\partial_i\hat{G}_{rr}^{p,h}(\mathbf{x}, \mathbf{x}_B, \omega)$
in V^e	$\hat{h}_{ii}(\mathbf{x}, \omega)$	0	$\delta(\mathbf{x} - \mathbf{x}_B)\delta_{ir}$
	$\hat{f}_i(\mathbf{x}, \omega)$	0	0
	$\hat{\tau}_{ij}(\mathbf{x}, \omega)$	$\hat{G}_{ij}^{\tau,q}(\mathbf{x}, \mathbf{x}_A, \omega)$	$\hat{G}_{ij,rr}^{\tau,h}(\mathbf{x}, \mathbf{x}_B, \omega)$
	$\hat{v}_i(\mathbf{x}, \omega)$	$\hat{G}_i^{v,q}(\mathbf{x}, \mathbf{x}_A, \omega)$	$\hat{G}_{i,rr}^{v,h}(\mathbf{x}, \mathbf{x}_B, \omega)$

346 where the superscripts p and q in the Green's functions on the left-hand side of equation 38 are respec-
 347 tively replaced by the elastodynamic pressure and source, \hat{p}^e and \hat{q}^e as both \mathbf{x}_A and \mathbf{x}_B are located
 348 within the solid. Similarly, the superscript p in the Green's functions on the right-hand side is replaced
 349 by \hat{p}^e , reflecting that \mathbf{x}_A is within the solid medium.

350 3.2.3 Point \mathbf{x}_A in the acoustic media V^a and \mathbf{x}_B in the solid media V^e

351 We now consider impulsive point sources of volume injection-rate density $\hat{q}(\mathbf{x}, \omega)$ at point \mathbf{x}_A in V^a
 352 for state A, and point impulsive sources of external deformation rate density $\hat{h}_{ij}(\mathbf{x}, \omega)$ at \mathbf{x}_B in V^e for
 353 state B. Table 4 summarizes the sources and corresponding wavefields in V^a and V^e for both states.
 354 Substituting the parameters from Table 3 into the convolution-type reciprocity relation 14 results in:

$$\begin{aligned}
 & \hat{G}_{rr}^{p,h}(\mathbf{x}_A, \mathbf{x}_B, \omega) - \hat{G}_{rr}^{\tau,q*}(\mathbf{x}_A, \mathbf{x}_B, \omega) \\
 = & \oint_{\partial V^a} \frac{-1}{j\omega\rho^a(\mathbf{x})} \left(\hat{G}^{p,q*}(\mathbf{x}, \mathbf{x}_A, \omega) \partial_i \hat{G}_{rr}^{p,h}(\mathbf{x}, \mathbf{x}_B, \omega) - \partial_i \hat{G}^{p,q*}(\mathbf{x}, \mathbf{x}_A, \omega) \hat{G}_{rr}^{p,h}(\mathbf{x}, \mathbf{x}_B, \omega) \right) n_i^a d^2\mathbf{x} \\
 & - \oint_{\partial V^e} \left(\hat{G}_i^{v,q*}(\mathbf{x}, \mathbf{x}_A, \omega) \hat{G}_{ij,rr}^{\tau,h}(\mathbf{x}, \mathbf{x}_B, \omega) + \hat{G}_{ij}^{\tau,q*}(\mathbf{x}, \mathbf{x}_A, \omega) * \hat{G}_{i,rr}^{v,h}(\mathbf{x}, \mathbf{x}_B, \omega) \right) n_j^e d^2\mathbf{x}.
 \end{aligned} \tag{58}$$

355 Using the source-receiver reciprocity relations 21-27, 29, and 30 on both sides of the equations gives,

$$\begin{aligned}
 & \hat{G}_{rr}^{p,h}(\mathbf{x}_A, \mathbf{x}_B, \omega) + \hat{G}_{rr}^{p,h*}(\mathbf{x}_A, \mathbf{x}_B, \omega) \\
 = & \oint_{\partial V^a} \frac{1}{j\omega\rho^a(\mathbf{x})} \left(\hat{G}^{p,q*}(\mathbf{x}_A, \mathbf{x}, \omega) \partial_i \hat{G}_{rr}^{\tau,q}(\mathbf{x}_B, \mathbf{x}, \omega) - \partial_i \hat{G}^{p,q*}(\mathbf{x}_A, \mathbf{x}, \omega) \hat{G}_{rr}^{\tau,q}(\mathbf{x}_B, \mathbf{x}, \omega) \right) n_i^a d^2\mathbf{x} \\
 & + \oint_{\partial V^e} \left(\hat{G}_i^{p,f*}(\mathbf{x}_A, \mathbf{x}, \omega) \hat{G}_{rr,ij}^{\tau,h}(\mathbf{x}_B, \mathbf{x}, \omega) + \hat{G}_{ij}^{p,h*}(\mathbf{x}_A, \mathbf{x}, \omega) \hat{G}_i^{p,f}(\mathbf{x}_B, \mathbf{x}, \omega) \right) n_j^e d^2\mathbf{x}.
 \end{aligned} \tag{59}$$

356 Applying summation notation and using the previously defined elastodynamic pressure p^e and its

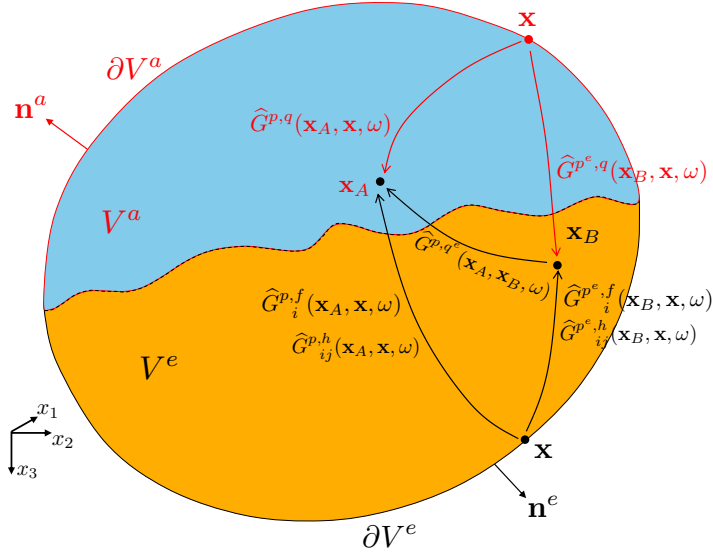


Figure 5. Pressure-type Green's function representation through interferometry when one receiver is in V^a and other in V^e . According to equation 60, the Green's function $\widehat{G}^{p,q^e}(\mathbf{x}_A, \mathbf{x}_B, \omega)$ can be obtained by cross-correlating the observations at \mathbf{x}_A and \mathbf{x}_B , and integrating along the source coordinate \mathbf{x} at ∂V^a and ∂V^e . The wavefields observed at \mathbf{x}_A and \mathbf{x}_B , along with the corresponding sources required at \mathbf{x} on ∂V^a and ∂V^e for Green's function $\widehat{G}^{p,q^e}(\mathbf{x}_A, \mathbf{x}_B, \omega)$ retrieval, are shown. Note that the rays in this figure represent the full responses between the source and receiver points, including primary and multiple scattering, as well as mode conversion due to inhomogeneities inside and outside the region $\partial V^a \cup \partial V^e$.

357 corresponding composite source q^e definitions at point \mathbf{x}_B yields,

$$\begin{aligned}
 & 2 \Re \left\{ \widehat{G}^{p,q^e}(\mathbf{x}_A, \mathbf{x}_B, \omega) \right\} \\
 = & \oint_{\partial V^a} \frac{-1}{j\omega\rho^a(\mathbf{x})} \left(\widehat{G}^{p,q^*}(\mathbf{x}_A, \mathbf{x}, \omega) \partial_i \widehat{G}^{p,q}(\mathbf{x}_B, \mathbf{x}, \omega) - \partial_i \widehat{G}^{p,q^*}(\mathbf{x}_A, \mathbf{x}, \omega) \widehat{G}^{p,q}(\mathbf{x}_B, \mathbf{x}, \omega) \right) n_i^a d^2\mathbf{x} \\
 & - \oint_{\partial V^e} \left(\widehat{G}_i^{p,f*}(\mathbf{x}_A, \mathbf{x}, \omega) \widehat{G}_{ij}^{p^e,h}(\mathbf{x}_B, \mathbf{x}, \omega) + \widehat{G}_{ij}^{p,h*}(\mathbf{x}_A, \mathbf{x}, \omega) * \widehat{G}_i^{p^e,f}(\mathbf{x}_B, \mathbf{x}, \omega) \right) n_j^e d^2\mathbf{x}.
 \end{aligned} \tag{60}$$

358 Figure 5 illustrates the Green's functions of the above equation observed at \mathbf{x}_A and \mathbf{x}_B , along with the
 359 corresponding sources required at \mathbf{x} on ∂V^a and ∂V^e to obtain the Green's function $\widehat{G}^{p,q^e}(\mathbf{x}_A, \mathbf{x}_B, \omega)$.
 360 This expression is analogous to equation 38, except that \widehat{p}^e and \widehat{q}^e at point \mathbf{x}_B are defined for the
 361 elastodynamic state. An expression similar to equation 50 can be written to approximate this Green's
 362 function, as was done in the previous section.

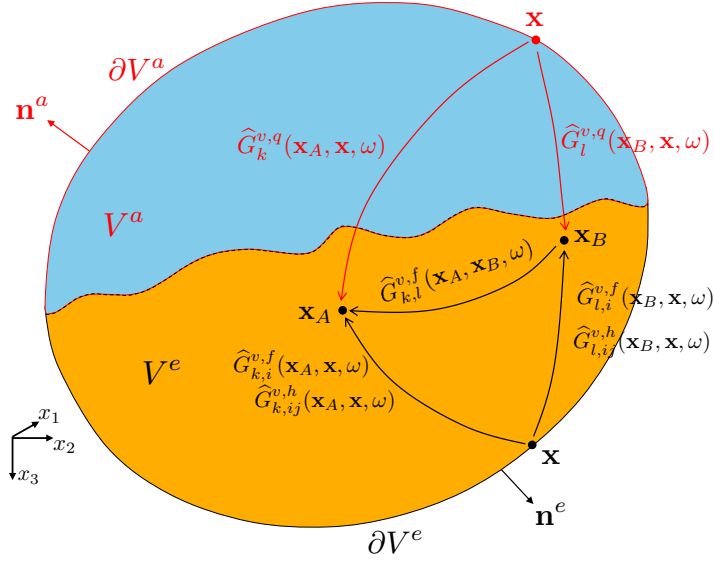


Figure 6. Illustration of interferometry by cross-correlation for the velocity Green's function representation when receivers are in V^e . According to equation 62, the Green's function $\widehat{G}_{k,l}^{v,f}(\mathbf{x}_A, \mathbf{x}_B, \omega)$ can be obtained by cross-correlating the observations at \mathbf{x}_A and \mathbf{x}_B , and integrating along the source coordinate \mathbf{x} at ∂V^a and ∂V^e . The wavefields observed at \mathbf{x}_A and \mathbf{x}_B , along with the corresponding sources required at \mathbf{x} on ∂V^a and ∂V^e for velocity Green's function retrieval, are shown. Note that the rays in this figure represent the full responses between the source and receiver points, including primary and multiple scattering, as well as mode conversion due to inhomogeneities inside and outside the region $\partial V^a \cup \partial V^e$.

3.3 Velocity Green's Function expression for seismic interferometry in coupled acoustic-elastic domain

To derive particle velocity Green's function expressions appropriate for SI, we keep points \mathbf{x}_A and \mathbf{x}_B in solid V^e (see Figure 6) and choose impulsive point force sources $\widehat{f}(\mathbf{x}, \omega)$ at both points; all other sources in V^e and V^a are set to zero. Table 5 summarizes the choice of sources along with the wavefields they generate in V^a and V^e for both states. Substituting parameters from Table 5 into the convolution-type reciprocity relation (equation 14) yields

$$\begin{aligned}
 & \widehat{G}_{l,k}^{v,f*}(\mathbf{x}_B, \mathbf{x}_A, \omega) + \widehat{G}_{k,l}^{v,f}(\mathbf{x}_A, \mathbf{x}_B, \omega) \\
 = & \oint_{\partial V^a} \frac{-1}{j\omega\rho^a(\mathbf{x})} \left(\widehat{G}_k^{p,f*}(\mathbf{x}, \mathbf{x}_A, \omega) \partial_i \widehat{G}_l^{p,f}(\mathbf{x}, \mathbf{x}_B, \omega) - \partial_i \widehat{G}_k^{p,f*}(\mathbf{x}, \mathbf{x}_A, \omega) \widehat{G}_l^{p,f}(\mathbf{x}, \mathbf{x}_B, \omega) \right) n_i^a d^2\mathbf{x} \\
 & - \oint_{\partial V^e} \left(\widehat{G}_{i,k}^{v,f*}(\mathbf{x}, \mathbf{x}_A, \omega) \widehat{G}_{ij,l}^{\tau,f}(\mathbf{x}, \mathbf{x}_B, \omega) + \widehat{G}_{ij,k}^{\tau,f*}(\mathbf{x}, \mathbf{x}_A, \omega) \widehat{G}_{i,l}^{v,f}(\mathbf{x}, \mathbf{x}_B, \omega) \right) n_j^e d^2\mathbf{x}.
 \end{aligned} \tag{61}$$

Applying source-receiver reciprocity of equations 21, 28 and 29 yields

Table 5. Choice of sources and wavefields in V^a and V^e for states A and B , when \mathbf{x}_A and \mathbf{x}_B are in V^e , to be used in the coupled convolution-type reciprocity theorem to derive velocity Green's function expression.

Domain	Parameter	State A	State B
in V^a	$\hat{q}(\mathbf{x}, \omega)$	0	0
	$\hat{f}_i(\mathbf{x}, \omega)$	0	0
	$\hat{p}(\mathbf{x}, \omega)$	$\hat{G}_k^{p,f}(\mathbf{x}, \mathbf{x}_A, \omega)$	$\hat{G}_l^{p,f}(\mathbf{x}, \mathbf{x}_B, \omega)$
	$\hat{v}_i(\mathbf{x}, \omega)$	$\frac{j}{\omega \rho^a(\mathbf{x})} \partial_i \hat{G}_k^{p,f}(\mathbf{x}, \mathbf{x}_A, \omega)$	$\frac{j}{\omega \rho^a(\mathbf{x})} \partial_i \hat{G}_l^{p,f}(\mathbf{x}, \mathbf{x}_B, \omega)$
in V^e	$\hat{h}_{ij}(\mathbf{x}, \omega)$	0	0
	$\hat{f}_i(\mathbf{x}, \omega)$	$\delta(\mathbf{x} - \mathbf{x}_A) \delta_{ik}$	$\delta(\mathbf{x} - \mathbf{x}_B) \delta_{il}$
	$\hat{\tau}_{ij}(\mathbf{x}, \omega)$	$\hat{G}_{ij,k}^{\tau,f}(\mathbf{x}, \mathbf{x}_A, \omega)$	$\hat{G}_{ij,l}^{\tau,f}(\mathbf{x}, \mathbf{x}_B, \omega)$
	$\hat{v}_i(\mathbf{x}, \omega)$	$\hat{G}_{i,k}^{v,f}(\mathbf{x}, \mathbf{x}_A, \omega)$	$\hat{G}_{i,l}^{v,f}(\mathbf{x}, \mathbf{x}_B, \omega)$

$$\begin{aligned}
& 2\Re \left\{ \hat{G}_{k,l}^{v,f}(\mathbf{x}_A, \mathbf{x}_B, \omega) \right\} \\
= & \oint_{\partial V^a} \frac{-1}{j\omega \rho^a(\mathbf{x})} \left(\hat{G}_k^{v,q*}(\mathbf{x}_A, \mathbf{x}, \omega) \partial_i \hat{G}_l^{v,q}(\mathbf{x}_B, \mathbf{x}, \omega) - \partial_i \hat{G}_k^{v,q*}(\mathbf{x}_A, \mathbf{x}, \omega) \hat{G}_l^{v,q}(\mathbf{x}_B, \mathbf{x}, \omega) \right) n_i^a d^2\mathbf{x} \\
& - \oint_{\partial V^e} \left(\hat{G}_{k,i}^{v,f*}(\mathbf{x}_A, \mathbf{x}, \omega) \hat{G}_{l,ij}^{v,h}(\mathbf{x}_B, \mathbf{x}, \omega) + \hat{G}_{k,ij}^{v,h*}(\mathbf{x}_A, \mathbf{x}, \omega) \hat{G}_{l,i}^{v,f}(\mathbf{x}_B, \mathbf{x}, \omega) \right) n_j^e d^2\mathbf{x}.
\end{aligned} \tag{62}$$

371 Figure 6 illustrates the Green's functions of the above equation observed at \mathbf{x}_A and \mathbf{x}_B , along with the
372 corresponding sources required at \mathbf{x} on ∂V^a and ∂V^e to obtain the Green's function $\hat{G}_{k,l}^{v,f}(\mathbf{x}_A, \mathbf{x}_B, \omega)$.
373 The above expression provides an exact representation of the elastodynamic Green's function in a
374 coupled system. However, similar to the case of the pressure Green's function, it is not particularly
375 useful in its current form due to the superposition of two correlation products under both integrals,
376 as well as the need for different source types on the boundary. To address this, we again approximate
377 the acoustic and elastic boundary integrals by adopting a similar approach and assumptions as in
378 the simplification of the pressure Green's function in Section 3.2.1. Assuming homogeneous material
379 properties at and outside of boundaries ∂V^a and ∂V^e leads to the following result:

$$\begin{aligned}
\Re \left\{ \hat{G}_{k,l}^{v,f}(\mathbf{x}_A, \mathbf{x}_B, \omega) \right\} \approx & \frac{1}{\rho^a c^a} \oint_{\partial V^a} \hat{G}_k^{v,q*}(\mathbf{x}_A, \mathbf{x}, \omega) \hat{G}_l^{v,q}(\mathbf{x}_B, \mathbf{x}, \omega) d^2\mathbf{x} \\
& + \frac{1}{\rho^e c^K} \oint_{\partial V^e} \hat{G}_{k,K}^{v,\phi*}(\mathbf{x}_A, \mathbf{x}, \omega) \hat{G}_{l,K}^{v,\phi}(\mathbf{x}_B, \mathbf{x}, \omega) d^2\mathbf{x}.
\end{aligned} \tag{63}$$

380 The above approximation is again highly accurate when ∂V^a and ∂V^e are portions of a sphere with a
381 sufficiently large radius, such that all rays are normal to ∂V^a and ∂V^e . In other cases, the approxima-
382 tion primarily introduces amplitude errors but correctly retrieves the phases of all arrivals. However, it

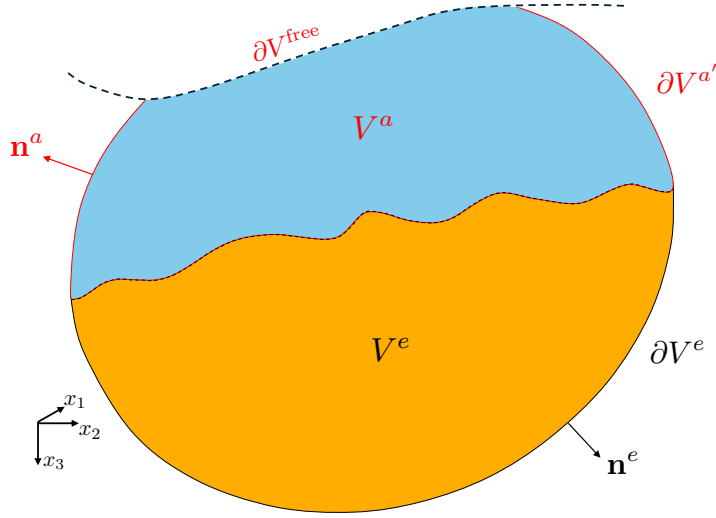


Figure 7. Modified configuration with a free surface ∂V^{free} .

383 may also lead to artifacts due to incomplete destructive interference of events, which would otherwise
 384 be fully cancelled when using the exact form in equation 62.

385 **3.4 Configuration with a free surface**

386 We consider a modified configuration (Figure 7) in which the closed surface is defined as $\partial V =$
 387 $\partial V^{a'} \cup \partial V^{\text{free}} \cup \partial V^e$. Here, ∂V^{free} represents a portion of the Earth's free surface, $\partial V^{a'}$ is an ar-
 388 bitrarily shaped surface enclosing part of the closed surface within the acoustic medium, and ∂V^e
 389 bounds the elastic solid part of the closed surface (see Figure 7). $\partial V^{a'}$ and ∂V^e do not necessarily
 390 coincide with a physical boundary. The observation points \mathbf{x}_A and \mathbf{x}_B are located within the volume
 391 enclosed by $\partial V^{a'} \cup \partial V^{\text{free}} \cup \partial V^e$. For this configuration, the results derived in the previous sec-
 392 tions for the pressure and velocity Green's functions can be directly applied. Because the acoustic
 393 pressure $p(\mathbf{x}, \omega)$ vanishes on ∂V^{free} , the integral $\oint_{\partial V^a}$ appearing in equations above need only
 394 be evaluated over $\partial V^{a'}$. Consequently, Green's functions $\widehat{G}^{p,q}(\mathbf{x}_A, \mathbf{x}_B, \omega)$ and $\widehat{G}_{k,l}^{v,f}(\mathbf{x}_A, \mathbf{x}_B, \omega)$ can
 395 be obtained by cross-correlating and integrating the responses of sources located solely on $\partial V^{a'}$ and
 396 ∂V^e ; no sources are needed on the free-surface boundary ∂V^{free} .

397 **4 UNCORRELATED AMBIENT SOURCES**

398 **4.1 Green's function through uncorrelated ambient sources**

399 The previous sections assumed that the sources on the boundaries ∂V^a and ∂V^e are impulsive point
 400 sources. However, many ocean-bottom SI studies (de Ridder & Dellinger 2011; Girard et al. 2023,

2024) rely on ambient sources. Therefore, in this section, we consider mutually uncorrelated ambient sources (Weaver & Lobkis 2001; Snieder 2004; Wapenaar 2004; Shapiro et al. 2005; Wapenaar & Fokkema 2006) acting on these boundaries.

We assume that ambient sources are acting on a closed surface $\partial V^a \cup \partial V^e$ (see Figure 1) with pressure-type sources on ∂V^a and P- and S-wave source type on ∂V^e . When all ambient sources act simultaneously, the observed particle velocity wavefield \hat{v}_k^{obs} at \mathbf{x}_A and \mathbf{x}_B can be expressed as

$$\hat{v}_k^{obs}(\mathbf{x}_A, \omega) = \int_{\partial V^a} \hat{G}_k^{v,q}(\mathbf{x}_A, \mathbf{x}, \omega) \hat{N}^q(\mathbf{x}, \omega) d^2\mathbf{x} + \int_{\partial V^e} \hat{G}_{k,K}^{v,\phi}(\mathbf{x}_A, \mathbf{x}, \omega) \hat{N}_K(\mathbf{x}, \omega) d^2\mathbf{x} \quad (64)$$

and

$$\hat{v}_l^{obs}(\mathbf{x}_B, \omega) = \int_{\partial V^a} \hat{G}_l^{v,q}(\mathbf{x}_B, \mathbf{x}', \omega) \hat{N}^q(\mathbf{x}', \omega) d^2\mathbf{x}' + \int_{\partial V^e} \hat{G}_{l,L}^{v,\phi}(\mathbf{x}_B, \mathbf{x}', \omega) \hat{N}_L(\mathbf{x}', \omega) d^2\mathbf{x}', \quad (65)$$

where $\hat{N}^q(\mathbf{x}, \omega)$ and $\hat{N}^q(\mathbf{x}', \omega)$ are the pressure-type not s at the boundary ∂V^a and $\hat{N}_K(\mathbf{x}, \omega)$, $\hat{N}_L(\mathbf{x}', \omega)$ are the ambient signal at the boundary ∂V^e , with $K, L = 0$ for a P-wave source and $K, L = 1, 2, 3$ for a S-wave source with different polarizations.

The continuous cross-correlation functions (CCFs), denoted as $\hat{C}_{k,l}^{v,v}$, of the ambient wavefield recordings $\hat{v}_k^{obs}(\mathbf{x}_A, \omega)$ and $\hat{v}_l^{obs}(\mathbf{x}_B, \omega)$ can be written as

$$\hat{C}_{k,l}^{v,v}(\mathbf{x}_A, \mathbf{x}_B, \omega) = \hat{v}_k^{obs*}(\mathbf{x}_A, \omega) \hat{v}_l^{obs}(\mathbf{x}_B, \omega). \quad (66)$$

Here, the notation $\hat{C}_{k,l}^{v,v}$ specifies the physical quantities being cross-correlated in the superscripts and their components in the subscripts. Substituting equations 64 and 65 into above yields

$$\begin{aligned} \hat{C}_{k,l}^{v,v}(\mathbf{x}_A, \mathbf{x}_B, \omega) &= \int_{\partial V^a} \int_{\partial V^a} \hat{G}_k^{v,q*}(\mathbf{x}_A, \mathbf{x}, \omega) \hat{G}_l^{v,q}(\mathbf{x}_B, \mathbf{x}', \omega) \hat{N}^{q*}(\mathbf{x}, \omega) \hat{N}^q(\mathbf{x}', \omega) d^2\mathbf{x} d^2\mathbf{x}' \\ &+ \int_{\partial V^a} \int_{\partial V^e} \hat{G}_k^{v,q*}(\mathbf{x}_A, \mathbf{x}, \omega) \hat{G}_{l,L}^{v,\phi}(\mathbf{x}_B, \mathbf{x}', \omega) \hat{N}^{q*}(\mathbf{x}, \omega) \hat{N}_L(\mathbf{x}', \omega) d^2\mathbf{x} d^2\mathbf{x}' \\ &+ \int_{\partial V^e} \int_{\partial V^a} \hat{G}_{k,K}^{v,\phi*}(\mathbf{x}_A, \mathbf{x}, \omega) \hat{G}_l^{v,q}(\mathbf{x}_B, \mathbf{x}', \omega) \hat{N}_K^*(\mathbf{x}, \omega) \hat{N}^q(\mathbf{x}', \omega) d^2\mathbf{x} d^2\mathbf{x}' \\ &+ \int_{\partial V^e} \int_{\partial V^e} \hat{G}_{k,K*}^{v,\phi}(\mathbf{x}_A, \mathbf{x}, \omega) \hat{G}_{l,L}^{v,\phi}(\mathbf{x}_B, \mathbf{x}', \omega) \hat{N}_K^*(\mathbf{x}, \omega) \hat{N}_L(\mathbf{x}', \omega) d^2\mathbf{x} d^2\mathbf{x}'. \end{aligned} \quad (67)$$

We assume that two ambient sources are mutually uncorrelated so that they obey

$$\langle \hat{N}^{q*}(\mathbf{x}, \omega) \hat{N}_L(\mathbf{x}', \omega) \rangle = \langle \hat{N}_K^*(\mathbf{x}, \omega) \hat{N}^q(\mathbf{x}', \omega) \rangle = 0. \quad (68)$$

However, same ambient-source types result in

$$\langle \hat{N}^{q*}(\mathbf{x}, \omega) \hat{N}^q(\mathbf{x}', \omega) \rangle = \frac{1}{\rho^a c^a} \delta(\mathbf{x} - \mathbf{x}') \hat{S}(\omega) \quad (69)$$

and

$$\langle \hat{N}_K^*(\mathbf{x}, \omega) \hat{N}_L(\mathbf{x}', \omega) \rangle = \frac{1}{\rho^e c^K} \delta_{KL} \delta(\mathbf{x} - \mathbf{x}') \hat{S}(\omega), \quad (70)$$

418 where $\langle \cdot \rangle$ denotes an ensemble average; and $\widehat{S}(\omega)$ is the ambient source power spectrum. All sources
 419 are assumed to have the same power spectra for all \mathbf{x} but different power normalization factors,
 420 $2/(\rho^a c^a)$ for \mathbf{x} at ∂V^a and $2/(\rho^e c^K)$ for \mathbf{x} at ∂V^e , respectively. Taking the ensemble average of
 421 equation 67 and accounting for equations 68-70, equation 67 yields the ensemble cross correlation

$$\begin{aligned}
 \langle \widehat{\mathcal{C}}_{k,l}^{v,v}(\mathbf{x}_A, \mathbf{x}_B, \omega) \rangle &= \frac{1}{\rho^a c^a} \int_{\partial V^a} \widehat{G}_k^{v,q*}(\mathbf{x}_A, \mathbf{x}, \omega) \widehat{G}_l^{v,q}(\mathbf{x}_B, \mathbf{x}, \omega) \widehat{S}(\omega) d^2 \mathbf{x} \\
 &+ \frac{1}{\rho^e c^K} \int_{\partial V^e} \widehat{G}_k^{v,\phi*}(\mathbf{x}_A, \mathbf{x}, \omega) \widehat{G}_l^{v,\phi}(\mathbf{x}_B, \mathbf{x}, \omega) \widehat{S}(\omega) d^2 \mathbf{x}.
 \end{aligned} \tag{71}$$

422 Combining this with equation 63 (considering the case when \mathbf{x}_A and \mathbf{x}_B lie within V^e) obtains

$$\Re\{\widehat{G}_{k,l}^{v,f}(\mathbf{x}_A, \mathbf{x}_B, \omega)\} S(\omega) \approx \langle \widehat{\mathcal{C}}_{k,l}^{v,v}(\mathbf{x}_A, \mathbf{x}_B, \omega) \rangle. \tag{72}$$

423 This relation suggests that the velocity CCFs due to uncorrelated ambient sources can be approxi-
 424 mated by the Green's function multiplied with the power spectra of the ambient sources, $\widehat{G}_{k,l}^{v,f}$ under
 425 the following conditions: the medium at and outside ∂V^a and ∂V^e is homogeneous; uniform pres-
 426 sure sources with strength $\sqrt{1/(\rho^a c^a)}$ are present at the boundary ∂V^a ; and uniform P- and S-wave
 427 ambient sources with strength $\sqrt{1/(\rho^e c^K)}$ are available at the boundary ∂V^e .

428 For the case where the CCF pertains to pressure, a similar convergence to the pressure Green's
 429 function can be derived

$$\Re\{\widehat{G}^{p,q}(\mathbf{x}_A, \mathbf{x}_B, \omega)\} S(\omega) \approx \langle \widehat{\mathcal{C}}^{p,p}(\mathbf{x}_A, \mathbf{x}_B, \omega) \rangle. \tag{73}$$

430 Although equations 72 and 73 demonstrate the recovery of interstation Green's functions through
 431 ambient cross correlations, their applicability to practical marine SI problems is limited due to hetero-
 432 geneous source distribution and the unavailability of sources of different types and at depths.

4.2 Modelling low-frequency ambient cross-correlation functions for ocean-bottom sensors

434 In practical marine scenarios, the conditions required for Green's function retrieval through cross-
 435 correlation functions (CCFs) are rarely satisfied primarily due to the absence of an ideal ambient
 436 source distribution. Ambient sources in oceanic regions predominantly originate from pressure fluctu-
 437 ations at the Earth's surface that are driven by interactions between wind-generated ocean storms and
 438 ocean-wave breaking, which induce pressure variations at the seafloor capable of generating seismic
 439 waves in the Earth. It is well known that these sources are often spatially non-uniform. Notably, there
 440 are no microseism sources within the solid Earth's volume itself. As a result, ambient sources caused
 441 by ocean-wave interactions at the surface, known as secondary microseisms, are typically modelled as
 442 non-zero pressure source distributions at the ocean surface and sources arising from the interaction of
 443 long-wavelength ocean waves with local bathymetry, referred to as primary microseisms, are approx-

444 imated as point force sources acting at the local bathymetry (Hasselmann 1963; Arduin & Herbers
445 2013; Arduin et al. 2015; Nakata et al. 2019).

446 We first derive the cross-correlation function (CCF) expression for ambient sources modelled as
447 point force sources acting on the ocean bottom. However, as mentioned above, these sources also can
448 be of a pressure-type acting at the ocean surface. Below, we also develop expressions for pressure-type
449 ambient sources. We refer this approach herein as cross-correlation modelling (CCM).

450 We may write the observed wavefield $\widehat{v}_k^{obs}(\mathbf{x}, \omega)$ due to ambient sources as

$$\widehat{v}_k^{obs}(\mathbf{x}, \omega) = \int_{\partial D} \widehat{G}_{k,n}^{v,f}(\mathbf{x}, \boldsymbol{\xi}, \omega) \widehat{N}_n(\boldsymbol{\xi}, \omega) d\boldsymbol{\xi}, \quad (74)$$

451 where $\widehat{N}_n(\boldsymbol{\xi}, \omega)$ denotes the n th component of the ambient force source; and ∂D is the region where
452 these sources are present, which in this case is the ocean bottom. Substituting equation 74 into equa-
453 tion 66 for observed wavefield recorded at \mathbf{x}_A and \mathbf{x}_B from ambient sources at $\boldsymbol{\xi}_1$ and $\boldsymbol{\xi}_2$, respectively,
454 results in the CCF expression

$$\widehat{\mathcal{C}}_{k,l}^{v,v}(\mathbf{x}_A, \mathbf{x}_B, \omega) = \iint_{\partial D} \widehat{G}_{k,n}^{v,f*}(\mathbf{x}_A, \boldsymbol{\xi}_1, \omega) \widehat{G}_{l,m}^{v,f}(\mathbf{x}_B, \boldsymbol{\xi}_2, \omega) \widehat{N}_n^*(\boldsymbol{\xi}_1, \omega) \widehat{N}_m(\boldsymbol{\xi}_2, \omega) d\boldsymbol{\xi}_1 d\boldsymbol{\xi}_2. \quad (75)$$

455 Usually, large numbers of windowed cross-correlations of continuous ambient wavefield recordings
456 are stacked to enhance coherent signals and downweight incoherent noise. We take the ensemble CCF
457 and assume that the ambient sources are uncorrelated as

$$\langle \widehat{N}_n^*(\boldsymbol{\xi}_1, \omega) \widehat{N}_m(\boldsymbol{\xi}_2, \omega) \rangle = \widehat{S}(\boldsymbol{\xi}_1, \omega) \delta_{nm} \delta(\boldsymbol{\xi}_1 - \boldsymbol{\xi}_2) \quad (76)$$

458 to simplify equation 75 to ensemble CCF

$$\langle \widehat{\mathcal{C}}_{k,l}^{v,v}(\mathbf{x}_A, \mathbf{x}_B, \omega) \rangle = \int_{\partial D} \widehat{G}_{k,n}^{v,f*}(\mathbf{x}_A, \boldsymbol{\xi}, \omega) \widehat{G}_{l,n}^{v,f}(\mathbf{x}_B, \boldsymbol{\xi}, \omega) \widehat{S}(\boldsymbol{\xi}, \omega) d\boldsymbol{\xi}, \quad (77)$$

459 where $\widehat{S}(\boldsymbol{\xi}, \omega)$ denotes the power-spectral density of the ambient source (Tromp et al. 2010). For a
460 narrow frequency band (e.g., 0.05-1.0 Hz), $S(\boldsymbol{\xi}, \omega)$ can be partitioned into its spatial and frequency
461 dependencies as

$$\widehat{S}(\boldsymbol{\xi}, \omega) = S(\boldsymbol{\xi}) \widehat{S}(\omega), \quad (78)$$

462 where the relative spatial distribution of ambient wavefield energy is defined such that $S(\boldsymbol{\xi}) = 0$ and
463 $S(\boldsymbol{\xi}) = 1$ represent effective sources with zero and the highest energy at location $\boldsymbol{\xi}$, respectively; and
464 $\widehat{S}(\omega)$ is the power spectrum of ambient wavefield sources. With these definitions, the CCF becomes

$$\langle \widehat{\mathcal{C}}_{k,l}^{v,v}(\mathbf{x}_A, \mathbf{x}_B, \omega) \rangle = \int_{\partial D} \widehat{G}_{k,n}^{v,f*}(\mathbf{x}_A, \boldsymbol{\xi}, \omega) \widehat{G}_{l,n}^{v,f}(\mathbf{x}_B, \boldsymbol{\xi}, \omega) S(\boldsymbol{\xi}) \widehat{S}(\omega) d\boldsymbol{\xi}, \quad (79)$$

465 or rearranging after using source-receiver reciprocity (equation 28):

$$\langle \widehat{\mathcal{C}}_{k,l}^{v,v}(\mathbf{x}_A, \mathbf{x}_B, \omega) \rangle = \int_{\partial D} \widehat{G}_{l,n}^{v,f}(\mathbf{x}_B, \boldsymbol{\xi}, \omega) \left\{ \left(\widehat{G}_{n,k}^{v,f*}(\boldsymbol{\xi}, \mathbf{x}_A, \omega) S(\boldsymbol{\xi}) \right) \widehat{S}(\omega) \right\} d\boldsymbol{\xi}. \quad (80)$$

466 Comparing the above with equation 74 and setting $\mathbf{x}_A = \mathbf{x}$ allows us to interpret the above expression
 467 as a correlation wavefield generated by the driving source,

$$\widehat{f}_n(\boldsymbol{\xi}, \mathbf{x}_A, \omega) = \widehat{G}_{n,k}^{v,f*}(\boldsymbol{\xi}, \mathbf{x}_A, \omega) S(\boldsymbol{\xi}) \widehat{S}(\omega), \quad (81)$$

468 also known as the ‘generating wavefield’ (Tromp et al. 2010). Because complex conjugation in the
 469 frequency domain is time-reversal in time domain, the ‘generating wavefield’ is simply the ambi-
 470 ent source-energy-weighted time-reversed wavefield recorded at ambient energy locations $\boldsymbol{\xi}$ due to a
 471 source at the virtual shot point locations \mathbf{x}_A with power spectrum $S(\omega)$. In the time domain, the above
 472 equation can be represented as

$$\langle \mathcal{C}_{k,l}^{v,v}(\mathbf{x}_A, \mathbf{x}_B, \tau) \rangle = \int_{\partial D} G_{l,n}^{v,f}(\mathbf{x}_B, \boldsymbol{\xi}, t) * \left\{ \left(G_{n,k}^{v,f}(\boldsymbol{\xi}, \mathbf{x}_A, -t) S(\boldsymbol{\xi}) \right) * S(t) \right\} (\tau) d\boldsymbol{\xi}, \quad (82)$$

473 where $*$ denote the convolution operator; $S(t)$ is ambient-source autocorrelation time function and τ
 474 is the temporal cross-correlation lag. Note the summation convention in the above equation, implying
 475 that the term on the right-hand side must be computed for $n = 1, 2, 3$, accounting for all the force
 476 components, to evaluate $\langle \mathcal{C}_{k,l}^{v,v} \rangle$, i.e.,

$$\begin{aligned} \langle \mathcal{C}_{k,l}^{v,v}(\mathbf{x}_A, \mathbf{x}_B, \tau) \rangle &= \int_{\partial D} G_{l,1}^{v,f}(\mathbf{x}_B, \boldsymbol{\xi}, t) * \left\{ \left(G_{1,k}^{v,f}(\boldsymbol{\xi}, \mathbf{x}_A, -t) S(\boldsymbol{\xi}) \right) * S(t) \right\} (\tau) d\boldsymbol{\xi} \\ &+ \int_{\partial D} G_{l,2}^{v,f}(\mathbf{x}_B, \boldsymbol{\xi}, t) * \left\{ \left(G_{2,k}^{v,f}(\boldsymbol{\xi}, \mathbf{x}_A, -t) S(\boldsymbol{\xi}) \right) * S(t) \right\} (\tau) d\boldsymbol{\xi} \\ &+ \int_{\partial D} G_{l,3}^{v,f}(\mathbf{x}_B, \boldsymbol{\xi}, t) * \left\{ \left(G_{3,k}^{v,f}(\boldsymbol{\xi}, \mathbf{x}_A, -t) S(\boldsymbol{\xi}) \right) * S(t) \right\} (\tau) d\boldsymbol{\xi}. \end{aligned} \quad (83)$$

477 For ambient-energy sources acting on ocean surface as distributed pressure sources, denoted by q , we
 478 may write equation 79 as

$$\langle \widehat{\mathcal{C}}_{k,l}^{v,v}(\mathbf{x}_A, \mathbf{x}_B, \omega) \rangle = \int_{\partial D} \widehat{G}_k^{v,q*}(\mathbf{x}_A, \boldsymbol{\xi}, \omega) \widehat{G}_l^{v,q}(\mathbf{x}_B, \boldsymbol{\xi}, \omega) S(\boldsymbol{\xi}) \widehat{S}(\omega) d\boldsymbol{\xi}. \quad (84)$$

479 Using source-reciprocity relation (equation 21) and arranging the above equation gives

$$\langle \widehat{\mathcal{C}}_{k,l}^{v,v}(\mathbf{x}_A, \mathbf{x}_B, \omega) \rangle = - \int_{\partial D} \widehat{G}_l^{v,q}(\mathbf{x}_B, \boldsymbol{\xi}, \omega) \left\{ \left(\widehat{G}_k^{p,f*}(\boldsymbol{\xi}, \mathbf{x}_A, \omega) S(\boldsymbol{\xi}) \right) \widehat{S}(\omega) \right\} d\boldsymbol{\xi}, \quad (85)$$

480 or equivalently in the time domain

$$\langle \mathcal{C}_{k,l}^{v,v}(\mathbf{x}_A, \mathbf{x}_B, \tau) \rangle = - \int_{\partial D} G_l^{v,q}(\mathbf{x}_B, \boldsymbol{\xi}, t) * \left\{ \left(G_k^{p,f}(\boldsymbol{\xi}, \mathbf{x}_A, -t) S(\boldsymbol{\xi}) \right) * S(t) \right\} (\tau) d\boldsymbol{\xi}. \quad (86)$$

481 For pressure CCFs when both receivers \mathbf{x}_A and \mathbf{x}_B are in water, similar time-domain equations
 482 can be written for ambient force sources

$$\langle \mathcal{C}^{p,p}(\mathbf{x}_A, \mathbf{x}_B, \tau) \rangle = - \int_{\partial D} G_n^{p,f}(\mathbf{x}_B, \boldsymbol{\xi}, t) * \left\{ \left(G_n^{v,q}(\boldsymbol{\xi}, \mathbf{x}_A, -t) S(\boldsymbol{\xi}) \right) * S(t) \right\} (\tau) d\boldsymbol{\xi}, \quad (87)$$

Table 6. Velocity model parameters for numerical example.

Domain	P-wave velocity c_P (m/s)	S-wave velocity c_S (m/s)	Density ρ (kg/m ³)	c_p gradient (km/s per km)	c_s gradient (km/s per km)
Water	1500	0	1000	-	-
Solid	1800	600	2100	0.40	0.23

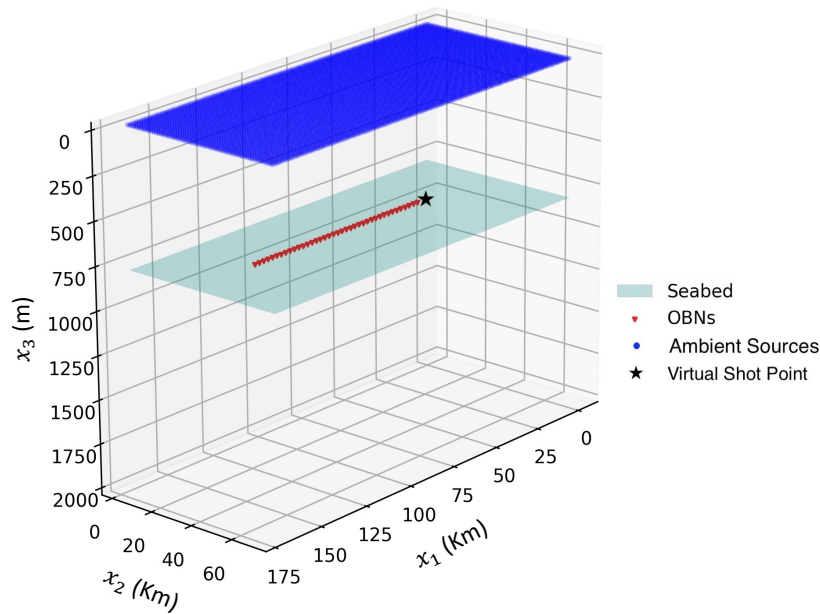
483 and for ambient pressure sources

$$\langle \mathcal{C}^{p,p}(\mathbf{x}_A, \mathbf{x}_B, \tau) \rangle = \int_{\partial D} G^{p,q}(\mathbf{x}_B, \boldsymbol{\xi}, t) * \{ \{ G^{p,q}(\boldsymbol{\xi}, \mathbf{x}_A, -t) S(\boldsymbol{\xi}) \} * S(t) \} (\tau) d\boldsymbol{\xi}. \quad (88)$$

484 Equations 82 and 86-88 enable the forward modelling of all (velocity and pressure) CCFs for dense
485 OBN arrays for different ambient source types, locations and configurations.

486 4.2.1 Numerical Example

487 We simulate the low-frequency vertical-velocity and pressure component cross-correlation wavefields,
488 $\langle \mathcal{C}_{3,3}^{v,v} \rangle$ and $\langle \mathcal{C}^{p,p} \rangle$, respectively, recorded on OBNs due to ambient sources acting on the ocean surface,
489 using their corresponding CCM modelling equations (equations 86 and 88, respectively). A detailed
490 workflow for implementing the CCM modelling equations (equations 82, and 86-88) in the time do-
491 main is described in Pandey et al. (2025). The synthetic ocean model is 176 km \times 76 km \times 14.6 km

**Figure 8.** Ambient sources, OBNs and virtual shot point location for results in Figure 9 and 10.

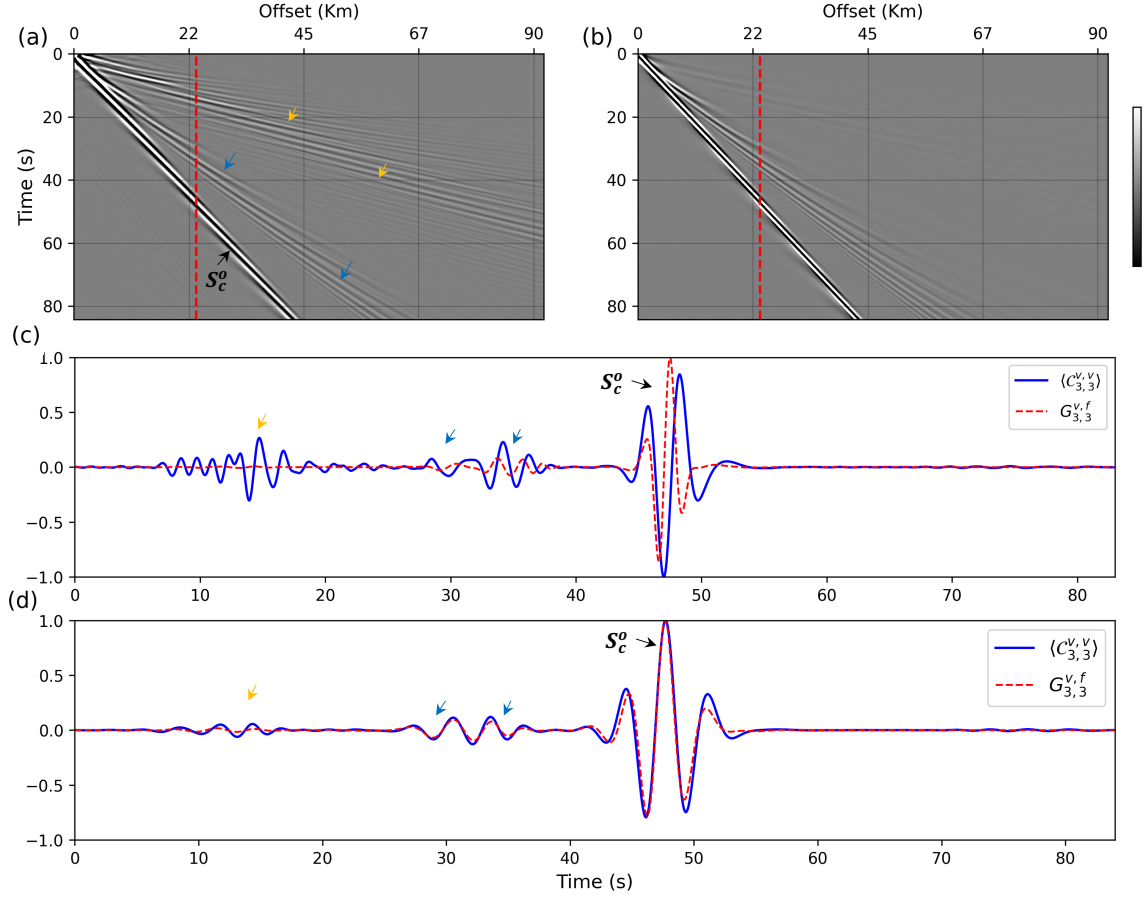


Figure 9. Vertical-component velocity: (a) VSG $\langle C_{3,3}^{v,v} \rangle$ and (b) Green's function, $G_{3,3}^{v,f}$, for the model shown in Figure 8. The relative amplitudes between shot gathers are not preserved. (c) Normalized traces from the location indicated by the red lines in (a) and (b). (d) Traces from (c), low-pass filtered to 0.35 Hz with $\langle C_{3,3}^{v,v} \rangle$ uniformly phase-shifted by $\pi/2$.

492 $(x_1 \times x_2 \times x_3)$ with a regular grid spacing of $0.4 \text{ km} \times 0.4 \text{ km} \times 0.2 \text{ km}$ ($dx_1 \times dx_2 \times dx_3$). We
 493 assume a flat seafloor with 0.8 km water depth and 1-D $c_P(x_3)$ and $c_S(x_3)$ velocity profiles beneath
 494 the ocean bottom. Table 6 presents the model properties where the c_P , c_S and ρ in the solid medium
 495 are defined at the ocean bottom and increase with depth according to the aforementioned gradients.
 496 The ambient source-time autocorrelation function $S(t)$ is a zero-phase Ricker wavelet with a 0.35 Hz
 497 central frequency. The time step for the simulation is 3.5 ms, with a 170 s total duration. With these
 498 parameters, the computational domain resolves a maximum frequency of 1.2 Hz. Figure 8 shows the
 499 geometry of ambient sources, OBNs and the virtual shot point location. The ambient sources are uni-
 500 formly distributed at each grid point across the ocean surface as pressure-type sources. The OBNs are
 501 located 10 m below the ocean bottom for $\langle C_{3,3}^{v,v} \rangle$ and 10 m above the ocean bottom for $\langle C_{3,3}^{p,p} \rangle$ along the
 502 x_1 -axis. The virtual shot point, indicated by a star, is located at $[x_1, x_2, x_3]_A = [48.0, 38.0, 0.81] \text{ km}$

503 for $\langle C_{3,3}^{v,v} \rangle$ and at $[x_1, x_2, x_3]_A = [48.0, 38.0, 0.79]$ km for $\langle C_{3,3}^{p,p} \rangle$. We use a free-surface top boundary
 504 with all other sides modelled as absorbing boundaries. We simulate forward wave propagation using
 505 SPECFEM3D Cartesian 4.1.0 (Komatitsch & Tromp 2002a,b; Komatitsch et al. 2023) published under
 506 the GPL3 license. The open-source software implements the 3-D spectral element method (Komatitsch
 507 et al. 2000) for wave propagation modelling.

508 Figure 9a presents the causal part of the simulated $\langle C_{3,3}^{v,v} \rangle$ VSG. Two distinct wave modes are
 509 evident: (1) the fundamental Scholte S_c^0 wave mode (black arrow) along with higher-order overtones
 510 (blue arrows); and (2) guided P waves (yellow arrows). These wave modes are consistent with field
 511 data VSG observations from the Gulf of Mexico, as reported in Girard et al. (2023, 2024). The S_c^0
 512 wave mode exhibits significantly higher energy compared to its higher-order modes and the guided P
 513 waves.

514 Figure 9b depicts the causal part of the vertical-component velocity Green's function, $G_{3,3}^{v,f}$, com-
 515 puted by injecting a vertical point force source at the virtual shot point location. In this case, the
 516 guided P waves are notably weaker than the S_c waves, and its higher-order modes are absent. Further-
 517 more, the fundamental and higher-order Scholte wave modes display a broader frequency bandwidth
 518 in comparison to those observed in $\langle C_{3,3}^{v,v} \rangle$.

519 Figure 9c provides a trace comparison at the location marked by the red line at an offset of 24
 520 km in Figures 9a and 9b. The amplitudes of both traces are normalized to unity. The comparison
 521 shows a phase discrepancy, as the main peaks exhibit misalignment between the Green's function and
 522 the $\langle C_{3,3}^{v,v} \rangle$ trace. Figure 9d shows the traces after low-pass filtering to 0.35 Hz, with $\langle C_{3,3}^{v,v} \rangle$ uniformly
 523 phase-shifted by $\pi/2$. Following this phase adjustment, the phases of the main peaks are better aligned.

524 Figure 10a shows the causal part of the pressure VSG $\langle C_{3,3}^{p,p} \rangle$. In this figure, the S_c^0 wave and
 525 its higher-order overtones (blue arrows) are weakly visible, while the guided P waves appear strong.
 526 Again, this observation is consistent with field-data $\langle C_{3,3}^{p,p} \rangle$ VSG examples from the Thunderhorse field
 527 OBN array in the Gulf of Mexico, where the ocean bottom, as seen by low frequency S_c^0 waves, is
 528 soft with average near-seafloor shear velocities of approximately 0.5–0.6 km/s (Girard et al. 2023). In
 529 contrast, the pressure Green's function, $G^{p,q}$, shown in Figure 10b, exhibits a clearly visible and strong
 530 S_c^0 mode along with higher-order modes. The red arrow in Figure 10a indicates spurious cross-mode
 531 events.

532 Figure 10c provides a trace comparison between $\langle C_{3,3}^{p,p} \rangle$ and $G^{p,q}$ at the location marked by the red
 533 lines in Figures 10a and 10b. Both traces are again normalized to unity. Similar to the observations
 534 above, S_c^0 and its higher-order mode are barely noticeable in the full frequency band and the main
 535 peaks of the guided P modes also show a misalignment between $\langle C_{3,3}^{p,p} \rangle$ and $G^{p,q}$. Figure 10d shows
 536 the traces after applying a 0.6 Hz low-pass filter, with $\langle C_{3,3}^{p,p} \rangle$ uniformly phase-shifted by $-\pi/2$. At this

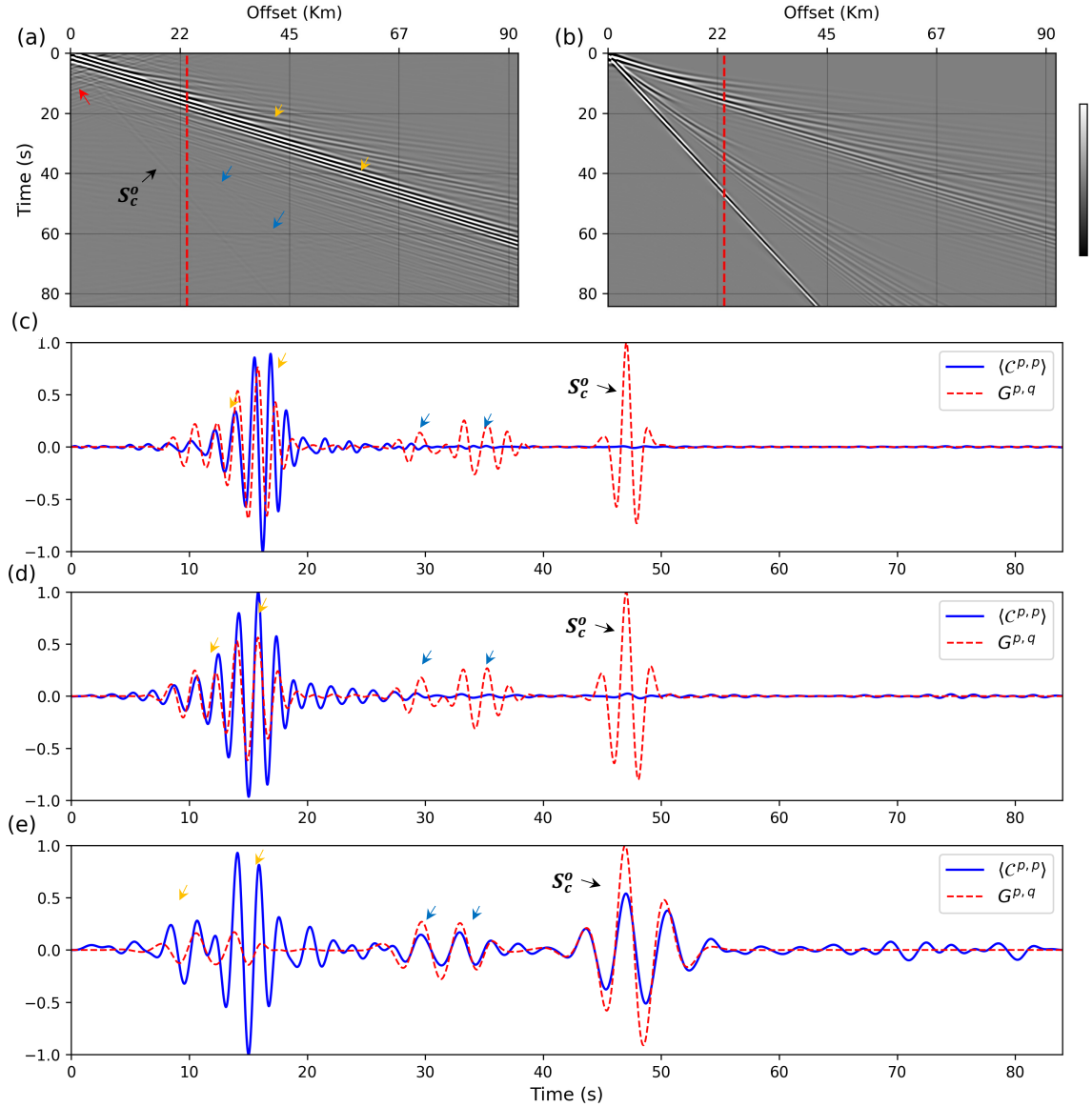


Figure 10. Pressure-component: (a) VSG, $\langle C^{p,p} \rangle$ and (b) Green's function, $G^{p,q}$, for the model shown in Figure 8. The relative amplitudes between shot gathers are not preserved. (c) Normalized traces from the location indicated by the red line in (a) and (b). (d) Traces from (c), low-passed to 0.6 Hz, with $\langle C^{p,p} \rangle$ uniformly phase-shifted by $-\pi/2$. (e) Traces from (d), further low-passed to 0.35 Hz.

537 stage, the phases of the main peaks of the guided P modes are better aligned; however, Scholte waves
 538 are still not visible at these frequencies. To further suppress the guided P modes, we again low-pass
 539 filter the traces to 0.35 Hz (Figure 10e). At this point, S_c^0 and its higher-order modes become more
 540 visible, and their main peaks align with $G^{p,q}$. However, more spurious events are observed due to
 541 cross-mode correlations and imperfect absorbing boundaries.

542 This example clearly illustrates: (1) the non-convergence of the cross-correlations to Green's func-

543 tions; and (2) the differential sensitivity of various components CCFs to different wave modes, using
544 a simple velocity model with flat bathymetry and uniform ambient sources on ocean surface. The re-
545 sults highlight the importance of modelling cross-correlations as self-consistent observations, rather
546 than as (exact or approximate) Green's functions, when the conditions required for SI Green's func-
547 tion retrieval are unmet. Significant phase differences are observed between various wave modes in
548 VSGs and the Green's function across different components. If not accurately accounting for these
549 differences, they could introduce significant errors in velocity model building through FWI using
550 cross-correlation gathers. Moreover, other key first-order control factors – such as the ambient energy
551 source mechanism and location, velocity heterogeneity (e.g., the presence of salt bodies), bathymetric
552 variations, and non-uniform ambient source distributions – also can significantly affect wave-mode
553 excitation and partitioning, further emphasizing the complexity of the problem and need for accurate
554 SI wavefield modelling solutions.

555 **5 CONCLUSIONS**

556 We derived reciprocity relations for coupled acoustic-elastic media using the constitutive equations
557 governing the coupling at the acoustic-elastic interface, as well as acoustic and elastodynamic reci-
558 procity theorems. From these derivations, we established source-receiver reciprocity expressions for
559 the coupled acoustic-elastic system. Subsequently, we provided an overview of the pressure and veloc-
560 ity Green's function representations in such systems, expressed in terms of wavefield cross correlations
561 at two observation points within arbitrarily heterogeneous lossless media. Both open and free-surface
562 configurations were considered. For the former, the wavefields are assumed to originate as sources
563 distributed along arbitrarily shaped boundaries enclosing the observation points. For the latter, it is
564 sufficient for sources to exist on an open surface that, together with the free surface, form a boundary
565 enclosing the observation points.

566 The pressure and velocity Green's function representations are exact but are not directly suitable
567 for SI applications. Specifically, this is because the integrand of these representations comprises a su-
568 perposition of four correlation products, two arising from the acoustic boundary integral and two from
569 the elastic boundary integral, that must be evaluated separately. The methodology also assumes the
570 availability of specific types of sources at all positions along the enclosing boundary: scalar monopole
571 and dipole sources on the acoustic boundary, and vector force and deformation sources on the elastic
572 boundary. Moreover, these sources are assumed to be impulsive point sources, which often do not
573 align with practical scenarios.

574 To address these challenges, we adopted a series of approximations to simplify the integrand into
575 two correlation product involving fewer source types. Specifically, monopole sources are used for both

576 states on the acoustic boundary, and monopole P- and S-wave sources were used for both states on the
 577 elastic boundary. We also discussed modifications for scenarios involving uncorrelated noise sources.
 578 In such cases, the representation integral reduces to a direct crosscorrelation of the recorded wavefields
 579 at two observation points. Finally, recognizing that ideal ambient source distributions rarely exist in
 580 practical scenarios, we develop modelling cross-correlation functions as self-consistent observations.
 581 This approach, referred to as cross-correlation modelling (CCM), only requires assuming uncorrelated
 582 ambient sources. It enables more realistic representations of cross correlations in field data from amb-
 583 bient wavefield studies. We present a synthetic example that simulates a vertical-velocity and pressure
 584 component cross-correlation wavefield using CCM, generated by ambient sources distributed across
 585 the ocean surface, and compare them with their corresponding Green's functions. Scholte waves are
 586 more prominent in the velocity VSGs, while in the pressure VSGs they are barely noticeable across
 587 the full frequency band. Additionally, there are significant phase differences between different wave
 588 modes identified in VSGs and Green's functions across different components, underscoring the im-
 589 portance of not treating cross-correlated data as Green's functions in the absence of the assumptions
 590 required for SI-based Green's function retrieval.

591 REFERENCES

- 592 Aki, K. & Richards, P. G., 2002. *Quantitative seismology*, University Science Books, 2nd edn.
- 593 Arduin, F. & Herbers, T. H., 2013. Noise generation in the solid Earth, oceans and atmosphere, from nonlinear
 594 interacting surface gravity waves in finite depth, *Journal of Fluid Mechanics*, **716**, 316–348.
- 595 Arduin, F., Gualtieri, L., & Stutzmann, E., 2015. How ocean waves rock the Earth: Two mechanisms explain
 596 microseisms with periods 3 to 300 s, *Geophysical Research Letters*, **42**(3), 765–772.
- 597 Bakulin, A. & Calvert, R., 2004. Virtual source: new method for imaging and 4D below complex overburden,
 598 in *SEG Technical Program Expanded Abstracts 2004*, pp. 2477–2480, SEG.
- 599 Bennethum, L. S., 2006. Compressibility moduli for porous materials incorporating volume fraction, *Journal*
 600 *of Engineering Mechanics*, **132**(11), 1205–1214.
- 601 Bojarski, N. N., 1983. Generalized reaction principles and reciprocity theorems for the wave equations, and
 602 the relationship between the time-advanced and time-retarded fields, *The Journal of the Acoustical Society of*
 603 *America*, **74**(1), 281–285.
- 604 De Hoop, A., 1966. An elastodynamic reciprocity theorem for linear, viscoelastic media, *Applied Scientific*
 605 *Research*, **16**, 39–45.
- 606 de Hoop, A. T., 1988. Time-domain reciprocity theorems for acoustic wave fields in fluids with relaxation,
 607 *The Journal of the Acoustical Society of America*, **84**(5), 1877–1882.
- 608 de Hoop, A. T., 1990. Reciprocity theorems for acoustic wave fields in fluid/solid configurations, *The Journal*
 609 *of the Acoustical Society of America*, **87**(5), 1932–1937.
- 610 de Ridder, S. & Dellinger, J., 2011. Ambient seismic noise eikonal tomography for near-surface imaging at
 611 Valhall, *The Leading Edge*, **30**(5), 506–512.

- 612 de Ridder, S. A. & Biondi, B. L., 2015. Ambient seismic noise tomography at Ekofisk, *Geophysics*, **80**(6),
613 B167–B176.
- 614 Fokkema, J. T. & van den Berg, P. M., 1993. *Seismic applications of acoustic reciprocity*, Elsevier Science
615 Publishing Company, Inc.
- 616 Girard, A., Shragge, J., Danilochkine, M., Udengaard, C., & Gerritsen, S., 2024. Observations from the
617 Seafloor: Ultra-low-frequency Ambient Ocean-Bottom Nodal Seismology at the Amendment Field, *Geo-*
618 *physical Journal International*, **239**(1), 17–36.
- 619 Girard, A. J., Shragge, J., & Olofsson, B., 2023. Low-frequency ambient ocean-bottom node surface-wave
620 seismology: A Gulf of Mexico case history, *Geophysics*, **88**(1), B21–B32.
- 621 Hasselmann, K., 1963. A statistical analysis of the generation of microseisms, *Reviews of Geophysics*, **1**(2),
622 177–210.
- 623 Knopoff, L. & Gangi, A. F., 1959. Seismic reciprocity, *Geophysics*, **24**(4), 681–691.
- 624 Komatitsch, D. & Tromp, J., 2002a. Spectral-element simulations of global seismic wave propagation—I.
625 Validation, *Geophysical Journal International*, **149**(2), 390–412.
- 626 Komatitsch, D. & Tromp, J., 2002b. Spectral-element simulations of global seismic wave propagation—II.
627 Three-dimensional models, oceans, rotation and self-gravitation, *Geophysical Journal International*, **150**(1),
628 303–318.
- 629 Komatitsch, D., Barnes, C., & Tromp, J., 2000. Wave propagation near a fluid-solid interface: A spectral-
630 element approach, *Geophysics*, **65**(2), 623–631.
- 631 Komatitsch, D., Tromp, J., Garg, R., Gharti, H. N., Nagaso, M., Oral, E., Peter, D., Afanasiev, M., Almada,
632 R., Ampuero, J. P., Bachmann, E., Bai, K., Basini, P., Beller, S., Bishop, J., Bissey, F., Blitz, C., Bottero, A.,
633 Bozdag, E., & Zhu, H., 2023. Specfem/specfem3d: Specfem3d v4.1.0.
- 634 Lobkis, O. I. & Weaver, R. L., 2001. On the emergence of the Green’s function in the correlations of a diffuse
635 field, *The Journal of the Acoustical Society of America*, **110**(6), 3011–3017.
- 636 Nakata, N., Gualtieri, L., & Fichtner, A., 2019. *Seismic Ambient Noise*, Cambridge University Press.
- 637 Pandey, A., Shragge, J., & Girard, A. J., 2025. First-order control factors for ocean-bottom ambient seismology
638 interferometric observations, Under review in *Geophysical Journal International*.
- 639 Rayleigh, J. W. S. B., 1878. *The theory of sound*, vol. 2, Dover Publications Inc., Reprint 1945.
- 640 Rickett, J. & Claerbout, J., 2000. Calculation of the sun’s acoustic impulse response by multi-dimensional
641 spectral factorization, *Solar Physics*, **192**, 203–210.
- 642 Sager, K., Ermert, L., Boehm, C., & Fichtner, A., 2018. Towards full waveform ambient noise inversion,
643 *Geophysical Journal International*, **212**(1), 566–590.
- 644 Sethi, H., Shragge, J., & Tsvankin, I., 2021. Mimetic finite-difference coupled-domain solver for anisotropic
645 media, *Geophysics*, **86**(1), T45–T59.
- 646 Shapiro, N. M., Campillo, M., Stehly, L., & Ritzwoller, M. H., 2005. High-Resolution Surface-Wave Tomog-
647 raphy from Ambient Seismic Noise, *Science*, **307**(5715), 1615–1618.
- 648 Snieder, R., 2004. Extracting the Green’s function from the correlation of coda waves: A derivation based on

- 649 stationary phase, *Physical Review E*, **69**(4), 046610.
- 650 Stewart, P., 2006. Interferometric imaging of ocean bottom noise, in *SEG International Exposition and Annual*
651 *Meeting*, pp. 1555–1559, SEG.
- 652 Sun, Y.-C., Zhang, W., Xu, J.-K., & Chen, X., 2017. Numerical simulation of 2-D seismic wave propagation in
653 the presence of a topographic fluid–solid interface at the sea bottom by the curvilinear grid finite-difference
654 method, *Geophysical Journal International*, **210**(3), 1721–1738.
- 655 Tromp, J., Luo, Y., Hanasoge, S., & Peter, D., 2010. Noise cross-correlation sensitivity kernels, *Geophysical*
656 *Journal International*, **183**(2), 791–819.
- 657 van Manen, D.-J., Curtis, A., & Robertsson, J. O., 2006. Interferometric modeling of wave propagation in
658 inhomogeneous elastic media using time reversal and reciprocity, *Geophysics*, **71**(4), SI47–SI60.
- 659 Wapenaar, C. & Haimé, G., 1990. Elastic extrapolation of primary seismic P- and S-waves, *Geophysical*
660 *Prospecting*, **38**(1), 23–60.
- 661 Wapenaar, C. P. A. & Berkhout, A. J., 1989. *Elastic wave field extrapolation*, Elsevier.
- 662 Wapenaar, K., 2004. Retrieving the elastodynamic Green’s function of an arbitrary inhomogeneous medium by
663 cross correlation, *Physical Review Letters*, **93**(254301), 1–4.
- 664 Wapenaar, K. & Fokkema, J., 2006. Green’s function representations for seismic interferometry, *Geophysics*,
665 **71**(4), SI33–SI46.
- 666 Weaver, R. L. & Lobkis, O. I., 2001. Ultrasonics without a Source: Thermal Fluctuation Correlations at MHz
667 Frequencies, *Physical Review Letters*, **87**(13), 134301.
- 668 Weaver, R. L. & Lobkis, O. I., 2004. Diffuse fields in open systems and the emergence of the Green’s function
669 (L), *The Journal of the Acoustical Society of America*, **116**(5), 2731–2734.